

A simple yet robust framework to estimate accurate daily mean land surface temperature from thermal observations of tandem polar orbiters

Falu Hong^a, Wenfeng Zhan^{a,b,*}, Frank-M. Götsche^c, Jiameng Lai^a, Zihan Liu^a, Leiqiu Hu^d, Peng Fu^e, Fan Huang^a, Jiufeng Li^a, Hua Li^f, Hua Wu^g

^a Jiangsu Provincial Key Laboratory of Geographic Information Science and Technology, International Institute for Earth System Science, Nanjing University, Nanjing, Jiangsu 210023, China

^b Jiangsu Center for Collaborative Innovation in Geographical Information Resource Development and Application, Nanjing, Jiangsu 210023, China

^c Karlsruhe Institute of Technology (KIT), Hermann-von-Helmholtz-Platz 1, 76344 Eggenstein-Leopoldshafen, Germany

^d Department of Atmospheric and Earth Science, The University of Alabama in Huntsville, Huntsville, AL 35805, USA

^e Department of Plant Biology, Carl R. Woese Institute for Genomic Biology, University of Illinois at Urbana-Champaign, Urbana, IL 61820, USA

^f Aerospace Information Research Institute, Chinese Academy of Sciences, China

^g State Key Laboratory of Resources and Environment Information System, Institute of Geographic Sciences and Natural Resources Research, Chinese Academy of Sciences, Beijing 100101, China

ARTICLE INFO

Edited by: Jing M. Chen

Keywords:

Land surface temperature
Thermal remote sensing
Sampling bias
Annual temperature cycle
Diurnal temperature cycle
Polar orbiters
MODIS

ABSTRACT

Remotely sensed and accurate daily mean land surface temperature (T_{dm}) is valuable for various applications such as air temperature estimation and climate change monitoring. However, most traditional methods employed by the remote sensing community estimate T_{dm} by averaging the – usually few – observed cloud-free land surface temperatures (LSTs). Such estimates can have large sampling bias, especially for tandem polar orbiters, due to their sparse sampling of diurnal LST dynamics and the unavailability of under-cloud LSTs. To estimate accurate T_{dm} based on thermal observations from tandem polar orbiters, here we propose a simple yet robust framework that combines the annual temperature cycle (ATC) and the diurnal temperature cycle (DTC) models (termed the ADTC-based framework). The ATC model is used to reconstruct daily instantaneous under-cloud LSTs, based on which the DTC model is employed to establish diurnally continuous LST dynamics for estimating T_{dm} . The proposed framework is validated with geostationary LST observations and in-situ thermal measurements under both cloud-free and overcast conditions. The validations show that, under cloud-free conditions, the ADTC-based framework is able to reduce the positive sampling bias obtained with simple averaging (> 2.0 K) and yields a mean absolute error (MAE) of approximately 0.5 K. Under overcast conditions, the ADTC-based framework yields MAEs of 1.0 K and 0.5 K at the daily and monthly scales, respectively. Furthermore, a contribution analysis indicates that the ATC model reduces the MAE from around 4.2 K to 2.0 K while the DTC model reduces the MAE from around 2.0 K to 1.0 K. Based on our validation results and tests performed with MODIS data, the presented simple yet robust ADTC-based framework is able to accurately estimate large-scale spatiotemporally continuous T_{dm} from thermal observations of tandem polar orbiters. Therefore, the ADTC-based framework is a potentially valuable tool for many related applications.

1. Introduction

Land surface temperature (LST) is a key variable that modulates land-atmosphere interactions (Li et al., 2013). Large-scale LST maps obtained by satellite thermal remote sensing have been widely used in various application scenarios (Anderson et al., 2008; Firozjaei et al.,

2020; Jin and Dickinson, 2010; Sims et al., 2008; Weng, 2009). Accurate ‘true’ daily mean LST (hereafter termed as T_{dm}), which can be calculated conceptually by averaging temporally continuous LSTs, is valuable in a number of applications such as frozen soil change modelling (Chen et al., 2017a; Zheng et al., 2020) and growing degree days mapping (Hassan et al., 2007). In addition, T_{dm} can be useful in surface air temperature estimation, surface property detection, evapotranspiration mapping,

* Corresponding author at: Nanjing University at Xianlin Campus, No. 163 Xianlin Avenue, Qixia District, Nanjing, Jiangsu 210023, China.

E-mail addresses: zhanwenfeng@nju.edu.cn (W. Zhan), frank.goetsche@kit.edu (F.-M. Götsche), leiqiu.hu@uah.edu (L. Hu), pengfu@illinois.edu (P. Fu), lihua@radi.ac.cn (H. Li), wuhua@igsnrr.ac.cn (H. Wu).

| Nomenclature | |
|------------------------------|--|
| Acronyms | |
| ATC | annual temperature cycle |
| ATCO | original annual temperature cycle |
| ATCE | enhanced annual temperature cycle |
| DTC | diurnal temperature cycle |
| DTR | daily temperature range |
| DOY | day of year |
| FOV | field-of-view |
| FY-2F VISSR | Visible Infrared Spin Scan Radiometer onboard FengYun-2F |
| LST | land surface temperature |
| MAE | mean absolute error |
| MB | mean bias |
| MERRA-2 | Modern-Era Retrospective analysis for Research and Applications version 2 |
| MODIS | Moderate Resolution Imaging Spectroradiometer |
| MSG-SEVIRI | the Spinning Enhanced Visible and Infrared Imager onboard Meteosat Second Generation |
| PMW | passive microwave |
| SEB | surface energy balance |
| SURFRAD | Surface Radiation Budget Network |
| <i>Symbol representation</i> | |
| T_{dm} | daily mean LST |
| $T_{dm_ATC_DTC}$ | daily mean LST calculated by frequently sampling |
| | diurnal LST dynamics modelled by DTC model with cloud-free LST observations and under-cloud LSTs reconstructed by ATC model |
| $T_{dm_ATC_four}$ | daily mean LST calculated by averaging cloud-free LST observations and under-cloud LSTs reconstructed by ATC model |
| $T_{dm_cloud_free}$ | daily mean LST calculated by averaging cloud-free LST observations |
| $T_{dm_obs_DTC}$ | daily mean LST calculated by frequently sampling diurnal LST dynamics modelled by DTC model with cloud-free and under-cloud LST observations |
| $T_{dm_obs_four}$ | daily mean LST calculated by averaging cloud-free and under-cloud LST observations |
| T_{dm_true} | true daily mean LST for validation |
| T_{in_ATC} | instantaneous under-cloud LSTs reconstructed by ATC model |
| $T_{in_ATC_DTC}$ | diurnal LST dynamics modelled by DTC model with cloud-free LST observations and under-cloud LSTs reconstructed by ATC model |
| $T_{in_cloud_free}$ | instantaneous cloud-free LST observations |
| T_{in_obs} | hourly LST observations |
| $T_{in_obs_DTC}$ | diurnal LST dynamics modelled by DTC model with cloud-free and under-cloud LST observations |
| $T_{in_under_cloud}$ | instantaneous under-cloud LST observations |
| ΔT_{sb} | sampling bias |

and global climatology analysis (Rao et al., 2019; Zhan et al., 2014; Zhang et al., 2021; Zhou and Wang, 2016). However, temporally continuous LSTs at both annual and diurnal scales required for estimating T_{dm} are not readily available, partly due to clouds, which causes frequently missing data (Duan et al., 2017; Li et al., 2018), and partly due to the sparse sampling of instantaneous satellite observation, which can be exacerbated by the tradeoff between the spatial and temporal resolutions (Sismanidis et al., 2017; Zhan et al., 2014).

Facing these challenges, studies often use temporally aggregated cloud-free LSTs (e.g., monthly aggregation) as a compromise (Chen et al., 2017b; Sobrino and Julien, 2013; Zheng et al., 2020; Zhou and Wang, 2016). However, temporally aggregated LSTs lack the daily variation information (Hassan et al., 2007). More importantly, the direct aggregation of cloud-free LSTs possesses two shortcomings: (1) under-cloud LSTs are simply ignored (Ermida et al., 2019; Langer et al., 2010; Westermann et al., 2012) and (2) only instantaneous LSTs at a few overpass times per daily cycle are used (Ouyang et al., 2012; Williamson et al., 2014). These shortcomings lead to an insufficient sampling of under-cloud LSTs and the continuous diurnal dynamics. Therefore, the direct aggregation of cloud-free LSTs can produce a significant sampling bias (ΔT_{sb}) compared to the ‘true’ T_{dm} (Chen et al., 2017b; Hu and Brunsell, 2013; Hu et al., 2020; Ouyang et al., 2012; Wang and Zhou, 2015), which can lead to deviations in trend analyses (Zhou and Wang, 2016).

Significant progress has been made towards the provision of T_{dm} (or the ΔT_{sb} estimation). T_{dm} estimation has been improved by incorporating temporally continuous LSTs established with diurnal temperature cycle (DTC) models (Ouyang et al., 2012; Hu et al., 2020). ΔT_{sb} has been estimated from under-cloud LSTs retrieved from passive microwave (PMW) observations or in-situ measurements (Ermida et al., 2019; Westermann et al., 2012); it also has been estimated via an empirical relationship with directly aggregated LSTs or surface air temperatures at the site scale (Hassan et al., 2007; Williamson et al., 2014; Zhou and Wang, 2016). However, these studies focused on either reconstructing temporally continuous cloud-free LSTs (Ouyang et al., 2012) or under-

cloud LSTs (Ermida et al., 2019; Westermann et al., 2012). In other words, approaches addressing these two issues simultaneously remain lacking, which hinders significantly the accurate estimation of T_{dm} (or the accurate correction of ΔT_{sb}).

According to the aforementioned analysis, a simple yet robust framework for estimating T_{dm} remains lacking. A framework for T_{dm} estimation should contain both of the two intermediate but indispensable processes, i.e., the reconstruction of under-cloud LSTs and the reconstruction of temporally continuous LSTs. In the following, we review the major methods used to implement these two processes.

Methods for reconstructing under-cloud LSTs can be divided into four categories: (1) statistical methods that are based on the relationships between cloud-free LSTs and associated predictors such as the elevation and vegetation index (Coops et al., 2007; Zhang et al., 2020b; Zhao et al., 2019); (2) surface energy balance (SEB) methods that are based on the physical relationship between shortwave radiation and LST (Jin, 2000; Martins et al., 2019; Zeng et al., 2018; Zhang et al., 2015; Zhang et al., 2017; Zhao and Duan, 2020); (3) PMW methods exploiting the small effects of clouds on microwave data (Duan et al., 2017; Holmes et al., 2015; Sun et al., 2019; Xu and Cheng, 2021; Zhang et al., 2019; Zhang et al., 2020a); and (4) annual temperature cycle (ATC) methods that combine multiple sinusoidal functions and short-term LST fluctuations estimated from meteorological observations or reanalysis data (Fu and Weng, 2016; Liu et al., 2019; Zou et al., 2018). Typical methods for reconstructing temporally continuous LSTs include downscaling, spatiotemporal fusion, and diurnal temperature cycle (DTC) modelling methods (Fu and Weng, 2016; Hong et al., 2018). Downscaling methods enhance high-frequency (e.g., geostationary) LST products to obtain continuous LSTs at fine spatial resolutions (Sismanidis et al., 2017; Zakšek and Oštir, 2012; Zhan et al., 2013; Zhan et al., 2016). Spatiotemporal fusion methods integrate LSTs from multiple sources, e.g., from geostationary satellites and polar orbiters, to fulfill this task (Long et al., 2020; Quan et al., 2018; Weng et al., 2014; Wu et al., 2015; Xia et al., 2019). DTC models fit instantaneous LSTs with physical diurnal models to obtain continuous diurnal LST dynamics (Hong et al., 2018).

The combination of any of the two methods listed above to reconstruct under-cloud and temporally continuous LSTs respectively offers the possibility to formulate a framework for T_{dm} estimation. However, the design of a simple yet robust framework that is easily implemented, driven by consistent data, and can potentially be applied globally remains a great challenge. For the reconstruction of under-cloud LSTs, the statistical and SEB methods are only suitable at the local scale, because their accuracies tend to decrease with the increasing size of a study area (Liu et al., 2019), while the PMW methods face disadvantages due to coarse spatial resolution, LST estimation influenced by a variable penetration depth, and observation gaps between orbits (Duan et al., 2017; Xu and Cheng, 2021; Zhang et al., 2020a). For reconstructing temporally continuous LST dynamics, downscaling and spatiotemporal fusion methods require geostationary LSTs as inputs: this limits their global use due to observation geometry and sensor differences between geostationary satellites (Xu et al., 2014). Extra difficulties can be posed by the relatively complex structure of these two methods (Quan et al., 2018) as well as the need to incorporate auxiliary data, which restricts a simple implementation (Wu et al., 2015; Zhan et al., 2013).

In contrast, the ATC and DTC models, which are able to reconstruct under-cloud and temporally continuous LSTs, respectively, can be combined to form a simple and robust framework for global T_{dm} estimation. These two models are also compactly structured, easily implemented, independent of auxiliary data (only data acquired from polar orbiters and reanalysis data are required), and globally applicable. Therefore, here we propose a framework that combines the ATC and DTC models (hereafter termed ‘ADTC-based framework’) to efficiently estimate T_{dm} . We then comprehensively evaluate the ADTC-based framework under cloud-free conditions with geostationary satellite data and under overcast conditions with in-situ measurements. The presented ADTC-based framework is an effective tool for estimating T_{dm} and, therefore, will be highly useful for a broad range of applications.

The paper is organized as follows: Section 2 introduces the selected datasets; Section 3 describes the ADTC-based framework (Section 3.1) and the associated validation strategy (Section 3.2). Section 4 presents the validation results (Sections 4.1 & 4.2), the individual contributions (Sections 4.3) and uncertainty analysis (Section 4.4) for each part of the ADTC-based framework, as well as discussions on the limitations and prospects of the ADTC-based framework (Section 4.5). The conclusions

are provided in Section 5.

2. Datasets

2.1. In-situ data

In-situ measurements from seven SURFRAD (Surface Radiation Budget Network) sites during 2010–2017 (see Fig. 1a) were used to validate the ADTC-based framework. Due to their rigorous quality control and continuity, SURFRAD measurements have long been used for the validation of satellite LST products (Duan et al., 2019; Guillevic et al., 2014; Guillevic et al., 2018; Martin et al., 2019; Wang and Liang, 2009). The seven SURFRAD sites are located in relatively heterogeneous areas where land cover types include grass, cropland, and bare soil. Broadband hemispherical radiances are measured with pyrgeometers (Eppley Precision Infrared Radiometer) with a wavelength range of 4–50 μm. Sensors at each site are mounted at a height of 10 m and have an effective field-of-view (FOV) radius of 30 to 45 m, resulting in an observed surface area of about 70 × 70 m². More detailed information on these seven sites is given in Table S1 in supplementary material. In-situ LSTs are estimated from the upward and downward longwave radiances measured at 1-min interval with the following formula (Duan et al., 2017; Ermida et al., 2020; Zhang et al., 2019):

$$T = \sqrt{\frac{L^{\uparrow} - (1 - \varepsilon_b)L^{\downarrow}}{\varepsilon_b\sigma}} \quad (1)$$

$$\varepsilon_b = 0.261 + 0.314\varepsilon_{31} + 0.411\varepsilon_{32}$$

where L^{\uparrow} and L^{\downarrow} are the upward and downward longwave radiation, respectively; σ is the Stefan-Boltzmann constant (5.67×10^{-8} W·m⁻²·K⁻⁴); ε_b is the broadband emissivity estimated from MODIS (Moderate Resolution Imaging Spectroradiometer) narrowband emissivities ε_{31} and ε_{32} in MODIS Channels 31 and 32, respectively (Liang et al., 2013). In order to reduce the impacts from outliers and short-term LST fluctuations, we first used the “3σ-Hampel identifier” to removes outliers, and then aggregated the 1-min LST observations to hourly values for validation (Duan et al., 2019).

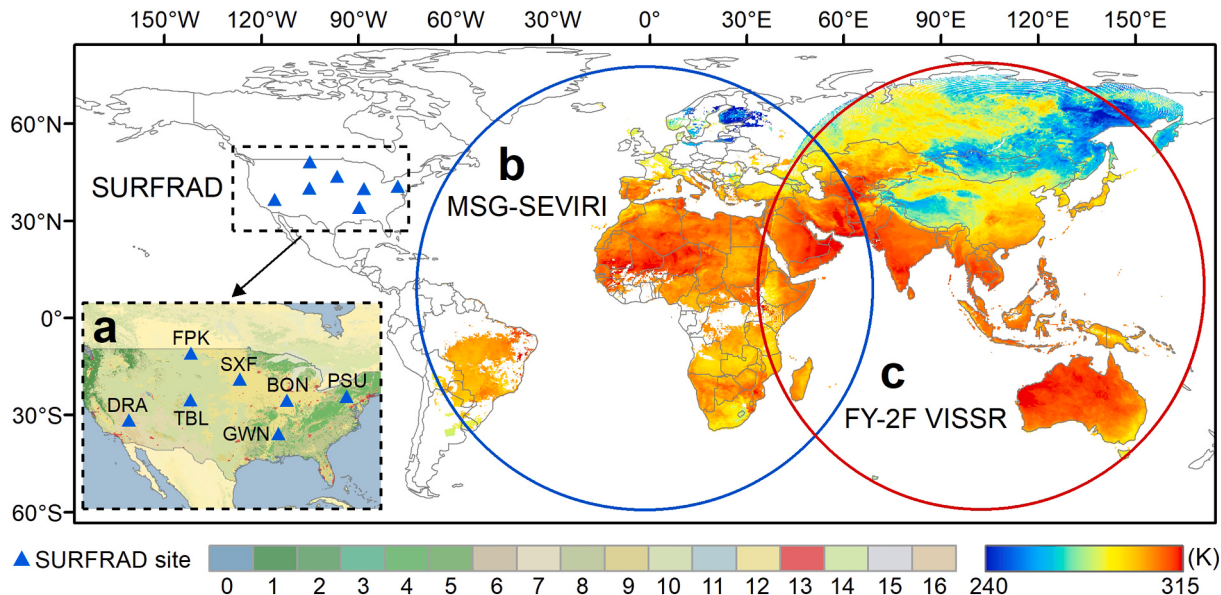


Fig. 1. Sites and areas used for validation. The locations of the seven SURFRAD sites are provided in (a). The spatial coverage of MSG-SEVIRI (Spinning Enhanced Visible and Infrared Imager onboard Meteosat Second Generation) and FY-2F VISSR (Visible Infrared Spin Scan Radiometer onboard FengYun-2F) are shown in (b) and (c), respectively. The continuous colour bar relates to the temporally aggregated LST of MSG/SEVIRI and FY-2F VISSR within the study period. The numbers ‘0’ to ‘16’ under the discrete colour bar refer to the land cover types of the International Geosphere-Biosphere Programme (IGBP, Friedl et al., 2002).

2.2. Satellite LST data

Two satellite LST datasets were employed, including MODIS and geostationary satellite data (see Table 1). The two satellite datasets were used for different purposes: MODIS data from 2010 to 2017 served as auxiliary data to provide LST-related information for each SURFRAD site. MODIS LST from July 15, 2018 were only input into the ADTC-based framework for illustrating the process of estimating T_{dm} (see Fig. S1). The geostationary satellite LSTs were used for validation under cloud free conditions, since they are able to provide temporally dense thermal observations of the surface that can be used to obtain realistic estimates of T_{dm} .

The MODIS data include the LST-related information from the MOD11A1 and MYD11A1 products in Collection 6. The accuracy of MODIS LST has been widely validated (Wan, 2014): here they were used to (1) provide the emissivity required for calculating SURFRAD LST, (2) provide cloud information for SURFRAD sites at MODIS overpass times, and (3) illustrate the estimation of T_{dm} with the ADTC-based framework (details are provided in Fig. S1).

The geostationary satellite data used in this study include LST products from MSG-SEVIRI (28 days in 2016) and FY-2F VISSR (2016) data (see Table 1). The spatial (temporal) resolutions of the MSG-SEVIRI and FY-2F LST data are 3 km (15 min) and 5 km (1 h), respectively. Comprehensive validations against in-situ measurements have shown that the RMSE of the operational MSG-SEVIRI LST product is generally between 1.0 K and 2.0 K (Götsche et al., 2016; Martin et al., 2019). While comprehensive validations against in-situ measurements are lacking for the FY-2F LST product, several assessments performed over a small number of sites indicate a RMSE of around 2.0 K, and FY-2F LSTs are in good agreement with the widely-validated MODIS LST products (Hu et al., 2018; Song et al., 2017).

2.3. Reanalysis data

The surface air temperatures (SATs) from MERRA-2 (the Modern-Era Retrospective analysis for Research and Applications version 2) reanalysis data (the specific collection name is inst1_2d_lfo_Nx) were used as auxiliary data to drive the ATC model (Gelaro et al., 2017). The spatial and temporal resolutions of these SAT data are $0.5^\circ \times 0.625^\circ$ and 1 h, respectively.

3. Methodology

3.1. The ADTC-based framework

3.1.1. Overview of the ADTC-based framework

In order to estimate accurate T_{dm} from thermal observations of tandem polar orbiters, the ADTC-based framework is implemented with

Table 1
Details of the satellite data used in this study.

| Sensor | Spatial extent | Temporal range | Product type | Product name ^c |
|------------|---------------------|----------------------------|--------------|---------------------------|
| MODIS | Pixels at each site | 2010–2017 | Emissivity | MYD11A1 |
| | h28v05 tile | July 15, 2018 ^a | LST | MOD11A1, MYD11A1 |
| FY-2F | Full disk | 2016 | LST | 1-h mean Full Disk LST |
| MSG-SEVIRI | Full disk | 28 days ^b | LST | LSA-001 |

^a The MODIS data from a single day (i.e., July 15, 2018) were only used as an example for illustrating the process of estimating T_{dm} (details in Fig. S1).

^b The selected days for MSG-SEVIRI data in 2016 are Jan. 1 to 7, Apr. 1 to 7, Jul. 1 to 7, and Oct. 1 to 7.

^c The data sources of these products are provided in Acknowledgements.

different strategies for overcast and cloud-free conditions. Overcast conditions are days when the diurnal LST dynamics is disturbed by clouds (including partly disturbed or blocked throughout a day), which is frequently the case and hinders thermal observations from satellites. In contrast, cloud-free conditions refer to days when LST observations at any overpass time within the LST diurnal cycle are cloud-free. Here, cloud-free conditions include not only standard cloud-free conditions, i.e., where all LST observations for a single day are cloud free, but also ‘synthetic’ cloud-free conditions, i.e., where valid LSTs at each overpass time are temporally aggregated, e.g., over a month or season, to eliminate the impact from cloud contamination (Hu et al., 2020). The latter is a common and well-established practice in the remote sensing community (Hong et al., 2018; Huang et al., 2016; Jin, 2000).

Under overcast conditions, the ADTC-based framework includes two major steps: the reconstruction of instantaneous under-cloud LSTs with the ATC model and the estimation of T_{dm} using the DTC model. Under cloud-free conditions, an adequate number of valid LSTs per day are available for DTC modelling and ATC modelling becomes unnecessary. Using MODIS (a typical thermal sensor onboard tandem polar orbiters) LSTs as an example, Fig. 2 illustrates how the ADTC-based framework estimates T_{dm} by performing the following four steps:

Step 1: Modelling intra-annual LST dynamics with the ATC model. For each overpass time, all valid MODIS LST observations and the auxiliary data (daily SATs from MERRA-2) (Fig. 2a) are used to drive the enhanced ATC model (see Section 3.1.1) to obtain the daily LST dynamics within an annual cycle.

Step 2: Reconstructing under-cloud LSTs with the ATC modelling results. The intra-annual LST dynamics reconstructed by the ATC model can be divided into cloud-free and under-cloud parts according to the validity of the original thermal observations (Fig. 2b). The modelled under-cloud LST are used to fill the gaps caused by cloud contamination. To drive the DTC model, the original MODIS cloud-free LSTs and the ATC modelling results are used together.

Step 3: Modelling diurnal LST dynamics with the DTC model. After Steps 1 & 2, the LSTs at the four overpass times are spatiotemporally continuous (see Fig. 2c). The four-parameter DTC model (see Section 3.1.2) is then employed to model diurnal LST dynamics (Fig. 2d).

Step 4: Estimating T_{dm} . Based on the diurnally continuous LSTs obtained in Step 3, T_{dm} can be estimated by averaging the frequently sampled LSTs (e.g., hourly or subhourly) or by integrating the DTC model function (Fig. 2e).

Under cloud-free conditions, only **Steps 3 & 4** are required to estimate T_{dm} (i.e., **Steps 1 & 2** related to the ATC model are unnecessary). Under overcast conditions, the ATC and DTC models are used sequentially to estimate T_{dm} , i.e., **Steps 1 to 4** are all required. Hereafter T_{dm} estimated by the ADTC-based framework is termed $T_{dm_ATC_DTC}$ under cloud-free as well as overcast conditions.

Note that when estimating T_{dm} directly from actual MODIS LST observations, the T_{dm} estimation mainly depends on the availability of valid LSTs. For the condition under which all four daily MODIS LST observations are valid, only **Steps 3 & 4** are required to estimate T_{dm} . However, this scenario may still not represent the true cloud-free condition since others times than the four MODIS transit times may still be cloudy. The uncertainties of ATC and DTC models as well as the accuracies of the ADTC-based framework under cloud-free and overcast conditions were discussed in the later section (Section 3.2 and Section 4).

3.1.2. Enhanced ATC model

This study employs the enhanced ATC model (termed the ATCE model) proposed by Zou et al., 2018 to estimate the daily LST dynamics within an annual cycle. Compared to the original ATC model (termed ATCO model), which describes the intra-annual LST dynamics with a single sinusoidal function (Bechtel, 2015), the ATCE model additionally incorporates daily SATs to capture day-to-day LST fluctuations. This enhances the modelling accuracy and simultaneously balances the

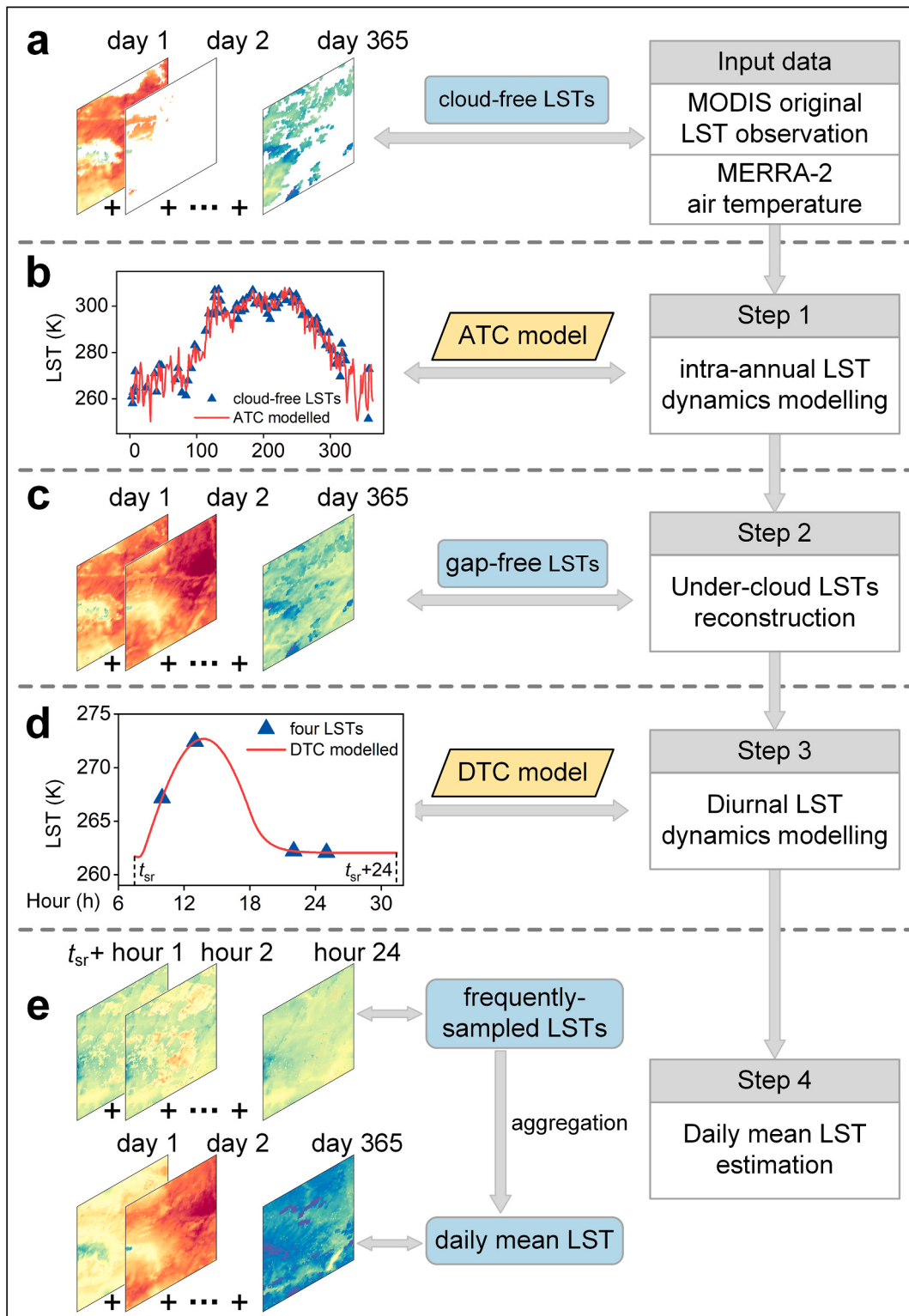


Fig. 2. Illustration of the ADTC-based framework for estimating accurate T_{dm} from MODIS data. The original MODIS observations (including auxiliary data), ATC-reconstructed results, and output T_{dm} are shown in subfigures (a), (c), and (e), respectively. Subfigures (b) and (d) illustrate the reconstruction procedures with the ATC and DTC models, respectively. t_{sr} denotes the sunrise time. An example of T_{dm} estimated with this framework is provided in Fig. S1.

model complexity (Liu et al., 2019). The ATCE model is given by the following equation.

$$\begin{cases} T_{\text{ATCE}}(d) = T_0 + A \sin\left(\frac{2\pi d}{N} + \theta\right) + k \cdot \Delta T_{\text{air}}(d) \\ T_{\text{ATCO}}(d) = T_{0,\text{air}} + A_{\text{air}} \sin\left(\frac{2\pi d}{N} + \theta_{\text{air}}\right) \\ \Delta T_{\text{air}}(d) = T_{\text{air}}(d) - T_{\text{ATCO}}(d) \end{cases} \quad (2)$$

where $T_{\text{ATCE}}(d)$ denotes the ATCE-modelled annual LST dynamics depending on the day of year (DOY, d); T_0 , A , and θ are the mean, amplitude and phase shift of the LST dynamics within an annual cycle, respectively; k is a multiplier used for modulating the difference between LST and SAT; $\Delta T_{\text{air}}(d)$ is the difference between the daily SATs (i.e., $T_{\text{air}}(d)$, obtained from reanalysis data or in-situ measurements for this study) and the modelled air temperatures $T_{\text{ATCO}}(d)$; $T_{0,\text{air}}$, A_{air} , and θ_{air} are the mean, amplitude and phase shift of the daily air temperature dynamics within an annual cycle, respectively; and N is the number of days in a year. The four parameters of the ATCE model (i.e., T_0 , A , θ , and k) can be solved by the MODIS LSTs and reanalysis SATs using the least-square method (Zou et al., 2018). Please note that there are systematic differences between MODIS LST and air temperature from reanalysis data or in-situ measurements. However, such biases are reduced to a large extent because only the day-to-day air temperature fluctuations are incorporated into the ATC model (i.e., $T_{\text{air}}(d)$) and the parameter k helps to modulate the difference between LST and air temperature (Liu et al., 2019).

3.1.3. Four-parameter DTC model

Since tandem polar orbiters provide at most four thermal observations per daily cycle, the modelling of diurnal LST dynamics requires a four-parameter DTC model. Here we use a well-performing four-parameter DTC model (termed GOT09-dT- τ model) derived from an advanced DTC model (Götsche and Olesen, 2009) with appropriate parameter reduction strategies (Hong et al., 2018). The GOT09-dT- τ model is formulated as follows:

$$\begin{cases} T_{\text{day}}(t) = T_0 + T_a \cos(\theta_z) \cos^{-1}(\theta_{z,\min}) \cdot e^{[m_{\min} - m(\theta_z)] \times 0.01}, & t < t_s \\ T_{\text{nig}}(t) = T_0 + T_a \cos(\theta_{zs}) \cos^{-1}(\theta_{z,\min}) \cdot e^{[m_{\min} - m(\theta_{zs})] \times 0.01} e^{\frac{-12}{4k}(\theta - \theta_s)}, & t \geq t_s \end{cases} \quad (3)$$

where $T_{\text{day}}(t)$ and $T_{\text{nig}}(t)$ are the LST dynamics for the day and at night, respectively; T_0 and T_a are the residual temperature and the diurnal amplitude, respectively; θ is the thermal hour angle; θ_z is the thermal zenith angle corresponding to θ ; $m(\theta_z)$ is the relative optical air mass; θ is denoted by θ_s when t equals to t_s (i.e., the time when free attenuation begins); when t equals t_m (time when LST reaches its daily maximum), θ_z is denoted by $\theta_{z,\min}$ and $m(\theta_z)$ by m_{\min} ; when t equals t_s , θ_z is denoted by θ_{zs} and $m(\theta_z)$ by $m(\theta_{zs})$; k is the attention rate of nighttime temperature decrease. Formulas for calculating θ , θ_z , $m(\theta_z)$, and k can be found in Götsche and Olesen (2009). For the GOT09-dT- τ model, there are only four parameters (i.e., T_0 , T_a , t_m , and t_s), which can be determined by fitting Eq. (3) to four daily thermal observations with the least-square method (Hong et al., 2018). Accurate T_{dm} can then be estimated by averaging the diurnally continuous LST dynamics provided by the GOT09-dT- τ model.

3.2. Validation strategy

Satellite LST products are usually validated by comparing them directly with in-situ measurements (Götsche et al., 2016; Guillevic et al., 2018; Li et al., 2014; Wang and Liang, 2009; Yang et al., 2020). However, the differences (or errors) between satellite and in-situ LSTs not only include the errors from their respective retrieval methods, but also contain the errors resulting from the mismatch in scale and field-of-

view (Ermida et al., 2014; Ermida et al., 2020; Guillevic et al., 2014; Li et al., 2020; Yu et al., 2019). Here, the differences (or errors) between satellite and in-situ LSTs also include errors of the ADTC-based framework, which all affects the T_{dm} estimation.

In other words, it would be difficult to differentiate between errors from the ADTC-based framework, LST retrieval and scale mismatch. It is even more challenging to separate the individual contributions and uncertainties from the ATC and DTC models embedded in the framework. To avoid this difficulty, this study evaluated the framework using LST datasets from a single source, i.e., modelling errors are investigated independently with either satellite data or in-situ measurements.

3.2.1. Validation strategy for cloud-free conditions

Under cloud-free conditions (i.e., the entire diurnal LST cycle is cloud-free), the ADTC-based framework is validated with thermal observations from geostationary satellites/sensors, including FY-2F and MSG-SEVIRI. These two geostationary satellites can provide hourly (FY-2F) or sub-hourly (15-min; MSG-SEVIRI) cloud-free LSTs, which – under standard cloud-free condition – cover an entire diurnal cycle well (Duan et al., 2012; Hong et al., 2018). Under cloud-free conditions, the daily averages of all hourly or sub-hourly cloud-free geostationary LSTs are, therefore, good approximations of ‘true’ daily mean LST.

To validate the ADTC-based framework under standard cloud-free conditions, days on which all geostationary hourly or sub-hourly LSTs are cloud-free are selected. i.e., the standard cloud-free days. The ‘true’ value of T_{dm} (termed $T_{\text{dm_true}}$) on a single day was calculated as the average of all hourly or sub-hourly cloud-free LSTs. The mean of the four LSTs at 01:30, 10:30, 13:30, and 22:30 (local solar time) represents the T_{dm} calculated with the traditional method (termed $T_{\text{dm_cloud_free}}$). For the same data, T_{dm} was also estimated with the ADTC-based framework for standard cloud-free conditions (termed $T_{\text{dm_ATC_DTC}}$). The difference between $T_{\text{dm_cloud_free}}$ and $T_{\text{dm_true}}$ (i.e., $T_{\text{dm_cloud_free}} - T_{\text{dm_true}}$) then represents the sampling bias (ΔT_{sb}) of the traditional method for calculating T_{dm} . The difference between $T_{\text{dm_ATC_DTC}}$ and $T_{\text{dm_true}}$, which is described using mean absolute error (MAE) and bias, reflects the accuracy of the ADTC-based framework. The improvement of $T_{\text{dm_cloud_free}} - T_{\text{dm_true}}$ relative to $T_{\text{dm_ATC_DTC}} - T_{\text{dm_true}}$ reflects the capability of the framework to reduce ΔT_{sb} .

The above-mentioned strategy is suitable for determining the accuracy of the ADTC-based framework under standard cloud-free condition. For validating the framework under synthetic cloud-free condition, we first obtained temporal LST composites by aggregating hourly or sub-hourly geostationary LST data pixel-wise at each overpass time over a specific month (or season). Apart from performing the validations per month (or season) rather than per day, the validation procedures are then identical for standard and synthetic cloud-free conditions. Considering that the pattern of diurnal LST dynamics after monthly or seasonal aggregation is very similar to that under standard cloud-free condition (Hong et al., 2018; Hu et al., 2020), the modelling accuracies under synthetic and standard cloud-free conditions are expected to be similar.

3.2.2. Validation strategy for overcast conditions

Under overcast conditions (i.e., the diurnal LST cycle is partly disturbed or diurnal LST observations are blocked by clouds throughout a day), only in-situ LSTs derived from SURFRAD measurements were used for validation, since in-situ measurements provide all-sky observations, including valid under-cloud LST measurements. Because SURFRAD in-situ measurements are temporally continuous, they can be used for estimating ‘true’ T_{dm} (i.e., $T_{\text{dm_true}}$) for validation. As already mentioned above, errors from LST retrieval and spatial scale mismatch can be excluded and, consequently, errors from the ADTC-based framework are isolated, if validations are performed with data from a single source (i.e., SURFRAD measurements).

Under overcast conditions, $T_{\text{dm_true}}$ can be straightforwardly estimated as the daily average of the temporally continuous in-situ LST

measurements (including both cloud-free and overcast conditions). T_{dm} estimated with the traditional method, i.e., $T_{dm_cloud_free}$, was obtained as the average of the in-situ cloud-free LST measurements coinciding with cloud-free MODIS overpasses (up to four possible observations per day). T_{dm} estimated with the ADTC-based framework, i.e., $T_{dm_ATC_DTC}$, was obtained from the cloud-free in-situ LSTs and some auxiliary data, e.g., in-situ SATs. Similar to the validation under cloud-free conditions, comparisons among SURFRAD-based T_{dm_true} , $T_{dm_cloud_free}$, and $T_{dm_ATC_DTC}$ provide information on the accuracy and ability of the ADTC-based framework to reduce ΔT_{sb} and estimate T_{dm} under overcast conditions.

3.2.3. Contributions from the ATC and DTC models to T_{dm} estimates

Under cloud-free conditions, applying the ATC model is unnecessary and the ADTC-based framework only uses the DTC model: as a result, contributions in estimating T_{dm} (or reducing ΔT_{sb}) only originate from the DTC model. In contrast, under overcast conditions, the ATC and DTC models both contribute significantly to the estimation of T_{dm} . To separate the contributions of the two models, we took the accuracy of $T_{dm_cloud_free}$ as the baseline (line ΔT_A in Fig. 3b). Here $T_{dm_cloud_free}$ represents the mean of all instantaneous cloud-free LST observations (mean of $T_{in_cloud_free}$, green circles in Fig. 3a). The accuracy improvements of the ATC and DTC models were then analyzed step by step.

The incorporation of the ATC model allows to fill LST gaps due to clouds (i.e., the instantaneous under-cloud LSTs T_{in_ATC} shown as blue triangles in Fig. 3a). The use of ATC-modelled T_{in_ATC} partly reduces ΔT_{sb} and ensures that four valid daily LSTs are available for the DTC model. In Fig. 3b, the accuracy improvement due to the ATC model (i.e.,

its contribution) is shown as the difference between $T_{dm_cloud_free}$ and $T_{dm_ATC_four}$ (mean of $T_{in_cloud_free}$ and T_{in_ATC}) with respect to the baseline, i.e., the difference between lines ΔT_A and ΔT_B . Furthermore, by substituting the reconstructed T_{in_ATC} with actually observed instantaneous under-cloud LSTs ($T_{in_under_cloud}$, red rectangles in Fig. 3a), the maximum contribution of under-cloud LST reconstruction can be reflected by the accuracy improvement from $T_{dm_cloud_free}$ to $T_{dm_obs_four}$ (mean of $T_{in_cloud_free}$ and $T_{in_under_cloud}$), i.e., the difference between lines ΔT_A and ΔT_C in Fig. 3b. The maximum contribution is reflected because the true instantaneous under-cloud LSTs ($T_{in_under_cloud}$) are obtained from measurements and are, therefore, the ideal results achieved by a model (including the ATC model). In other words, the difference between $T_{dm_ATC_four}$ and $T_{dm_obs_four}$ (i.e., between lines ΔT_B and ΔT_C in Fig. 3b) reflects the uncertainty added to the estimation of T_{dm} when reconstructing under-cloud LSTs with the ATC model.

With the four daily LSTs consisting of the original instantaneous cloud-free observations ($T_{in_cloud_free}$) and the instantaneous under-cloud LSTs reconstructed by the ATC model (T_{in_ATC}), the fitting of the DTC model becomes feasible. The DTC model provides continuous diurnal LST dynamics ($T_{in_ATC_DTC}$, blue line in Fig. 3a) for estimating T_{dm} . Therefore, the specific contribution of the DTC model to the accuracy improvement can be quantified as the difference between $T_{dm_ATC_four}$ and $T_{dm_ATC_DTC}$ (mean of $T_{in_ATC_DTC}$), i.e., between lines ΔT_B and ΔT_D in Fig. 3b. Similarly, the contribution of the DTC model is partly reflected in the difference between lines ΔT_C and ΔT_E in Fig. 3b, i.e., the accuracy improvement from $T_{dm_obs_four}$ to $T_{dm_obs_DTC}$, with the latter being the daily mean of the frequently-sampled $T_{in_obs_DTC}$ (red line in Fig. 3a) obtained by fitting the DTC model to the in-situ LST observations. Furthermore, the difference between $T_{dm_ATC_DTC}$ and $T_{dm_obs_DTC}$ (i.e., between lines ΔT_D and ΔT_E in Fig. 3b) reflects the robustness of the DTC model to ATC modelling error.

Table 2 summarizes the aforementioned six T_{dm} (termed the six LSTs) for comprehensively evaluating the separate contributions of the ATC and DTC model, with T_{dm_true} used as the reference. The ΔT_{sb} of the traditional method for estimating T_{dm} is reflected by the error of $T_{dm_cloud_free}$ (line ΔT_A in Fig. 3b). The improvement contributed by the

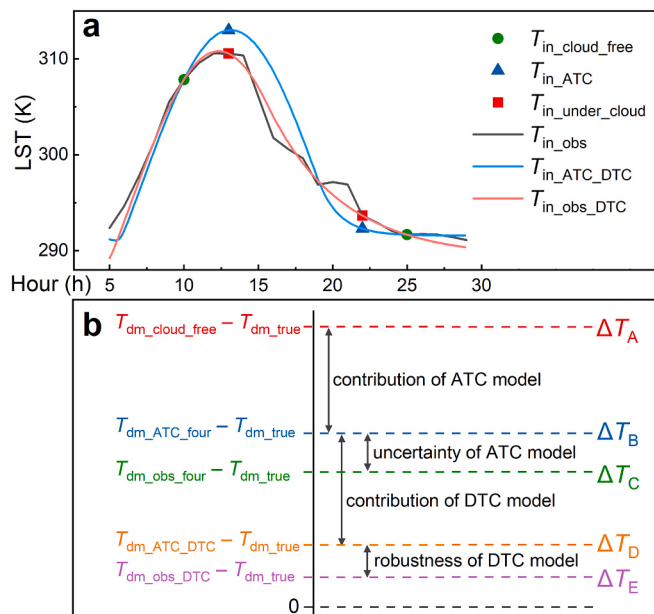


Fig. 3. The instantaneous and daily mean LSTs involved in the comparison and validation of the ADTC-based framework under overcast condition. The instantaneous LSTs based on which daily mean LSTs are estimated are illustrated in (a). Noting that the value along the x-axis >24 denotes time of the next day. Points shown by the green circles, red rectangles, and blue triangles represent cloud-free observations, under-cloud observations, and temperatures reconstructed by the ATC model, respectively. The black, red, and blue lines indicate in-situ LSTs, temperatures reconstructed by the DTC model based on the cloud-free and under-cloud observations, and temperatures reconstructed by the DTC model based on the cloud-free observations and ATC-modelled results, respectively. The six estimates of daily mean LSTs (details provided in Table 2) used for validating and quantifying the separate contributions from the ATC and DTC models are displayed in (b) where their respective differences are labeled as ΔT_A to ΔT_E . (For interpretation of the references to colour in this figure legend, the reader is referred to the web version of this article.)

Table 2
The six different estimates of daily mean LST T_{dm} used in the comparisons.

| Daily mean LST estimates | Definition | Presentation in Fig. 3 | Explanation/Comment |
|--------------------------|--|---|---|
| T_{dm_true} | mean of hourly LSTs | mean of T_{in_obs} (black line) | 'true' value of daily mean LST for validation |
| $T_{dm_cloud_free}$ | mean of cloud-free LSTs | mean of $T_{in_cloud_free}$ (green points) | traditional method for estimating T_{dm} |
| $T_{dm_ATC_four}$ | cloud-free LSTs + ATC model + mean of four overpassing LSTs ^a | mean of $T_{in_cloud_free}$ and T_{in_ATC} (green and blue points) | used to quantify the contribution of the ATC model |
| $T_{dm_obs_four}$ | cloud-free LSTs + under-cloud LSTs + mean of the four overpassing LSTs | mean of $T_{in_cloud_free}$ and $T_{in_under_cloud}$ (green and red points) | used to quantify the maximum contribution of under-cloud LST reconstruction as well as the uncertainty of the ATC model |
| $T_{dm_ATC_DTC}$ | cloud-free LSTs + ATC model + DTC model | mean of $T_{in_ATC_DTC}$ (blue line) | T_{dm} estimated by the ADTC-based framework, also used to reflect the contribution of the DTC model |
| $T_{dm_obs_DTC}$ | cloud-free LSTs + under-cloud LSTs + DTC model | mean of $T_{in_obs_DTC}$ (red line) | used to reflect the robustness of the DTC model |

^a "+" means the combination of data and models to estimate T_{dm} .

ATC model and its modelling uncertainty are expressed by the differences of $T_{dm_ATC_four}$ and $T_{dm_obs_four}$ with respect to T_{dm_true} (lines ΔT_B and ΔT_C). Similarly, the improvement contributed by the DTC model and its modelling robustness are expressed by the differences of $T_{dm_ATC_DTC}$ and $T_{dm_obs_DTC}$ with respect to T_{dm_true} (lines ΔT_D and ΔT_E).

3.2.4. Uncertainties of the ATC and DTC models

Under cloud-free condition, only the DTC model is required to estimate T_{dm} ; and the uncertainties of the DTC model can therefore be denoted directly by the accuracies of the ADTC-based framework. Under overcast condition, the accuracies of the T_{dm} estimated by the ADTC-based framework are closely related to the uncertainties of both the ATC and DTC models, i.e., the errors in reconstruction of instantaneous under-cloud LSTs with the ATC model as well as the errors in the reconstruction of diurnally continuous LST dynamics with the DTC model. It is not easy to separate the individual uncertainties from these two models because the DTC and ATC models are intertwined in the ADTC-based framework. Similar to the separation of the individual contributions of the ATC and DTC models, here we quantify their uncertainties step by step only with in-situ measurements.

Using the under-cloud in-situ LST observations ($T_{in_under_cloud}$ in Fig. 3), the uncertainties of the ATC model (T_{in_ATC} in Fig. 3) are directly quantifiable. Based on the ATC-reconstructed LSTs, the DTC modelling becomes feasible. The errors of the DTC-modelled LSTs ($T_{in_ATC_DTC}$ in Fig. 3), which also reflect the uncertainties of the DTC modelling when facing the uncertainties from the ATC modelling and short-term LST fluctuations under various cloud-contaminated conditions, are consequently quantifiable with the hourly in-situ LST observations (T_{in_obs} in Fig. 3). The comparison of error between the $T_{in_ATC_DTC}$ (instantaneous temperature) and $T_{dm_ATC_DTC}$ (daily mean temperature) indicates the robustness of the DTC model in estimating T_{dm} .

4. Results and discussion

4.1. Validation under cloud-free conditions

The validation results of the ADTC-based framework under cloud-free conditions with FY-2F and MSG-SEVIRI data are provided in Fig. 4. The numbers of standard cloud-free days (Fig. 4a and b) indicate that under-cloud LSTs need to be reconstructed over most regions except deserts, where standard cloud-free days are generally more frequent.

For each standard cloud-free day, we calculate both the sampling bias ($T_{dm_cloud_free} - T_{dm_true}$) and the error of the generated T_{dm} ($T_{dm_ATC_DTC} - T_{dm_true}$) as well as their mean values. The results show that the sampling bias (ΔT_{sb}) is always positive and in most regions exceeds 2.0 K (Fig. 4c and d). These results confirm that the average of the four LSTs from polar orbiters per daily cycle is unable to estimate T_{dm} accurately. Within a standard or synthetic cloud-free diurnal cycle, the LSTs sampled at 10:30 and 13:30 (local solar time) are close to the daily maximum, while LST sampled at 22:30 and 01:30 (local solar time) are typically slightly higher than the daily minimum, which usually occurs around sunrise (Crosson et al., 2012; Good, 2015). This indicates that the gradual nighttime cooling is probably under-sampled by the four daily LSTs for accurately estimating T_{dm} . For this reason, $T_{dm_cloud_free}$ usually overestimates the more accurate T_{dm} estimate that is obtained from hourly (or minutely) observations, i.e., ΔT_{sb} is positive for $T_{dm_cloud_free}$.

Spatial variations of ΔT_{sb} (see Fig. 4c and d) show that it is related to land cover type and climate zone. ΔT_{sb} is generally higher in dry climates under which the surface is dominated by bare soils (e.g., the Sahara Desert and Tibetan Plateau). From the perspective of temporal sampling, ΔT_{sb} is expected to be positively correlated with daily temperature range (DTR): a low ΔT_{sb} (i.e., $T_{dm_cloud_free}$ is close to actual T_{dm}) is usually associated with a small DTR (i.e., a small diurnal variation of LST) and vice versa. Under dry climates the relatively large DTR, therefore, often increases ΔT_{sb} .

The results show that the mean bias (MB) and MAE of $T_{dm_ATC_DTC}$ are around -0.1 K and 0.5 K, respectively (see Fig. 4e and f). Moreover, these errors are insensitive to location and land cover type, which indicates that under cloud-free conditions the ADTC-based framework is able to reduce ΔT_{sb} and consequently produces high-quality estimates of T_{dm} .

4.2. Validation under overcast conditions

4.2.1. Sampling biases (ΔT_{sb}) at daily and monthly scales

For cloud-free conditions, the results in Section 4.1 show that T_{dm} estimated directly as the average of the available cloud-free satellite LSTs (i.e., $T_{dm_cloud_free}$) is systematically higher than the actual ('true') T_{dm} . Using SURFRAD data, we calculate the ΔT_{sb} between $T_{dm_cloud_free}$ and true daily/monthly mean LSTs (T_{dm_true}) under overcast conditions. Fig. 5 and Fig. 6 illustrate that the respective ΔT_{sb} have different patterns at daily and monthly scales.

At the daily scale, $T_{dm_cloud_free}$ is calculated by averaging the limited number of available cloud-free observations in a single day (ranging from 0 to 4 for MODIS observations), while T_{dm_true} is calculated by averaging temporally continuous diurnal LST dynamics. Consequently, the ΔT_{sb} depends on the frequency and time of the day when clouds occur. Fig. 5 shows that the pattern of ΔT_{sb} at the daily scale differs greatly for the sixteen cases (Fig. 5b) that were defined based on the availability of the four daily LST observations. ΔT_{sb} is usually positive when clouds block nighttime LST observations (Fig. 5a) and can exceed 5.0 K if LST observations at night are unavailable. The opposite occurs for invalid daytime observations. If we only consider Case 1 (four valid LST observations), ΔT_{sb} remains larger than 2.0 K. Furthermore, the low proportion of Case 1 (20%, see Fig. 5c) means that for most days, there are fewer than four cloud-free LST observations to drive the DTC model, which stresses the necessity of reconstructing under-cloud LST.

At the monthly scale, $T_{dm_cloud_free}$ is calculated by directly averaging all discrete and instantaneous cloud-free observations within the specific month. The frequency and time of the day of cloud cover have less impact on the value of ΔT_{sb} than that at the daily scale. Fig. 6 displays that ΔT_{sb} is always positive (usually larger than 2.0 K) and close to the MAE at the monthly scale. This is because monthly aggregation results in a similar pattern of diurnal LST dynamics as under cloud-free conditions. Therefore, ΔT_{sb} at the monthly scale is very similar to that under cloud-free conditions at the daily scale (Section 4.1) or similar to Case 1 (with four valid daily LSTs) at the daily scale (Fig. 5a).

The differences in ΔT_{sb} between daily and monthly scales indicate that a validation of the framework under overcast conditions should consider the time scale of the temporal aggregation. Therefore, in the following we validate daily and monthly time-scales separately.

4.2.2. Validation at the daily scale

The validations at the daily scale in Fig. 7 show that the ADTC-based framework is able to reduce the ΔT_{sb} ($T_{dm_cloud_free} - T_{dm_true}$) and fill the gaps caused by clouds. In the following, we describe the two main improvements in detail.

First, the validations indicate that the ADTC-based framework achieves a stable and systematic improvement of ΔT_{sb} at the daily scale (Fig. 7). The MAE and bias of $T_{dm_cloud_free}$ exceed 2.0 K for most cases (see Fig. 5a). In contrast, the errors of $T_{dm_ATC_DTC}$ are less than those of $T_{dm_cloud_free}$: MAE and bias of $T_{dm_ATC_DTC}$ are reduced considerably to around 1.0 and -0.4 K, respectively. Moreover, the error of $T_{dm_ATC_DTC}$ is insensitive to the season, which is probably due to the robustness of the selected DTC model (GOT09-dT- τ) in estimating T_{dm} for all cases (see Section 4.4).

Second, the ADTC-based framework is able to fill the gaps caused by clouds. The proportion of days with fewer than four valid observations (i.e., Cases 2 to 16) is about 80% within 30-day intervals except for the DRA site (gray shadows in Fig. 7). Furthermore, the proportion of days with four invalid observations (i.e. Case 16) is 27% (see Fig. 5c). Clouds

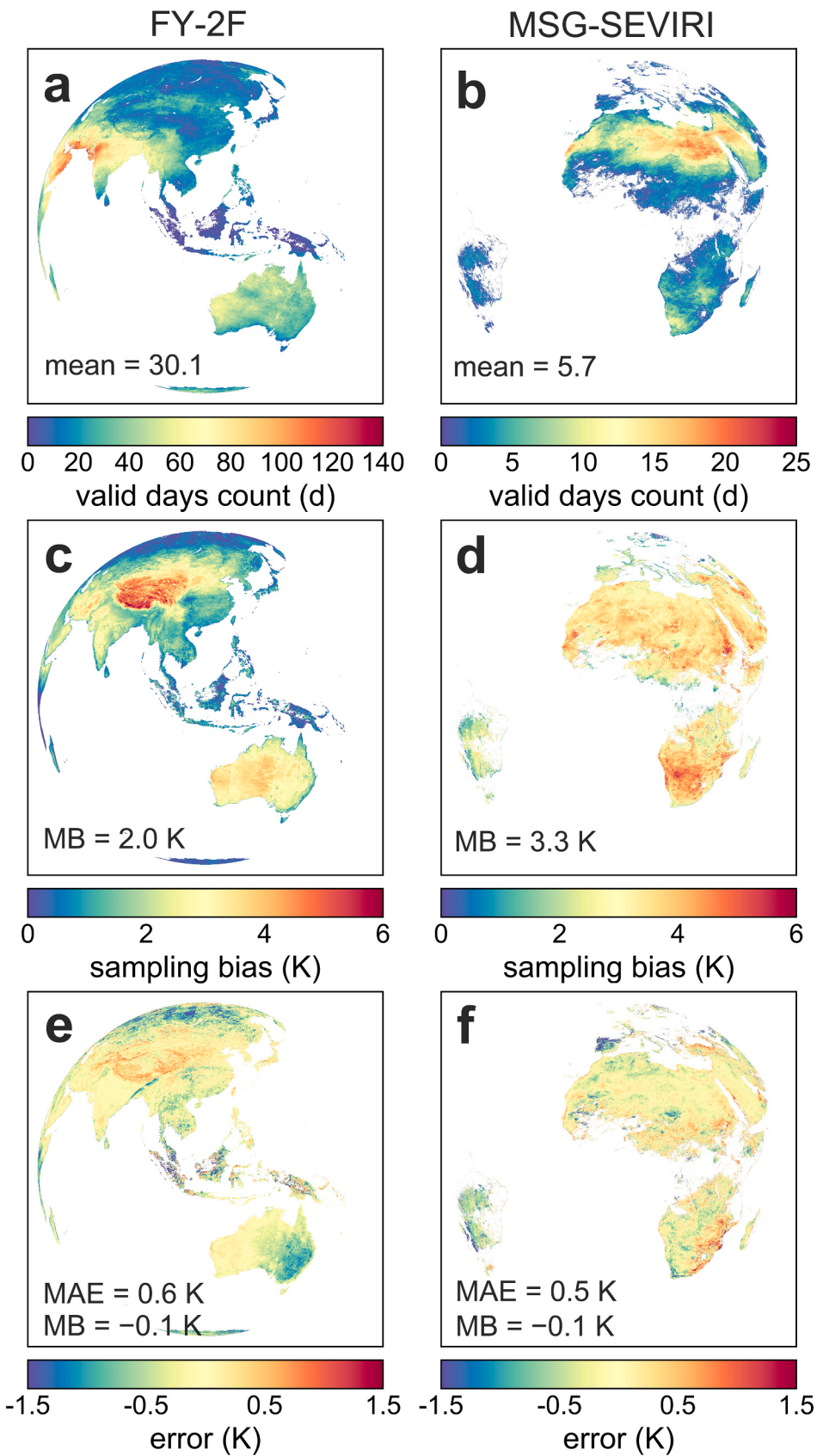


Fig. 4. Validation results under cloud-free conditions for geostationary satellite LSTs. The first and second columns show results for FY-2F and MSG-SEVIRI, respectively. (a) and (b) show the number of standard cloud-free days in the study period with the number denoting the average count of standard cloud-free days. (c) and (d) show the mean daily sampling bias ($T_{dm_cloud_free} - T_{dm_true}$). (e) and (f) show the error ($T_{dm_ATC_DTC} - T_{dm_true}$) of the ADTC-based framework.

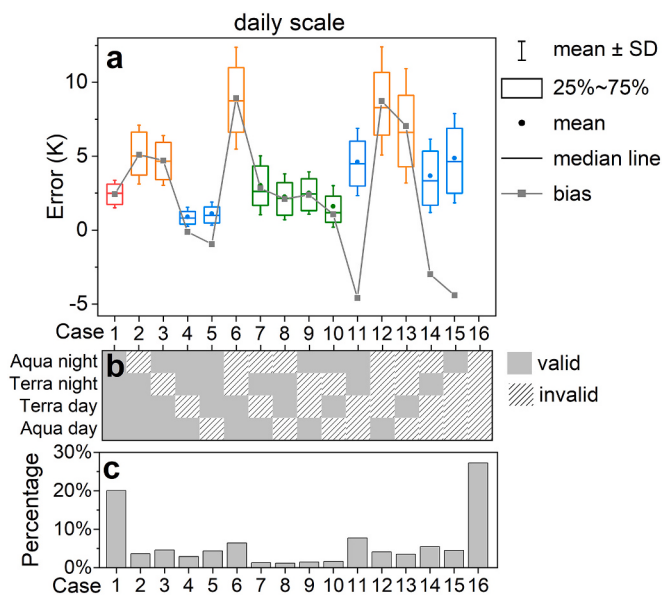


Fig. 5. Sampling bias ($T_{dm_cloud_free} - T_{dm_true}$) at the daily scale obtained from all SURFRAD data. (a) displays MAEs (boxplots) and biases (gray line) of $T_{dm_cloud_free} - T_{dm_true}$ for the sixteen cases illustrated in (b). Red colour represents four valid LSTs per daily cycle. Orange, green, and blue indicate that there are more than, equal, and fewer valid LST observations during the day than at night, respectively. No value for Case 16 is provided because in this case, all four daily observations are invalid. (c) displays the percentage of each case. (For interpretation of the references to colour in this figure legend, the reader is referred to the web version of this article.)

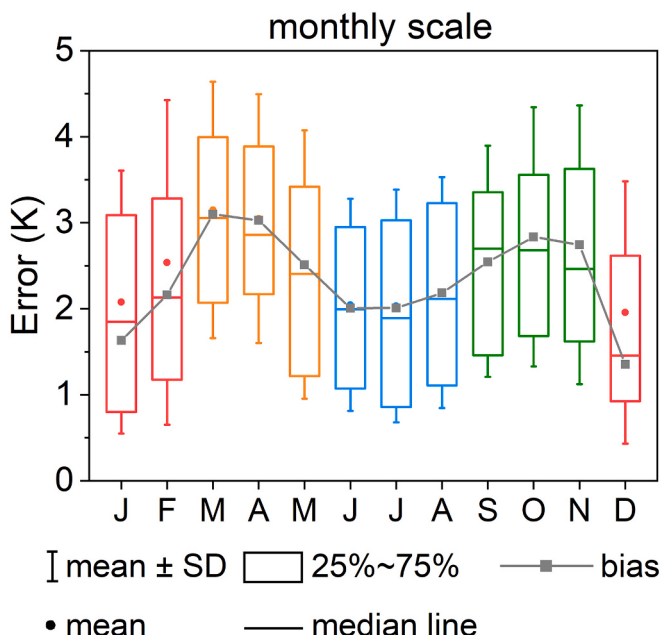


Fig. 6. Sampling bias ($T_{dm_cloud_free} - T_{dm_true}$) at the monthly scale obtained from all SURFRAD data. Red, orange, blue, and green represent winter, spring, summer, and autumn, respectively. (For interpretation of the references to colour in this figure legend, the reader is referred to the web version of this article.)

cause frequent gaps in the results of $T_{dm_cloud_free}$ (discrete red points in Fig. 7). In contrast, the results of $T_{dm_ATC_DTC}$ are spatiotemporally continuous (continuous purple lines in Fig. 7). The flowchart of the ADTC-based framework (Fig. 2) and testing with MODIS data (Fig. S1)

illustrates the process of generating spatiotemporally continuous T_{dm} : the ATC model reconstructs the under-cloud LSTs to ensure that there are four valid LSTs per day to drive the DTC model, which yields spatiotemporally continuous $T_{dm_ATC_DTC}$.

4.2.3. Validation at the monthly scale

The errors of T_{dm} cloud free and $T_{dm_ATC_DTC}$ with T_{dm_true} as reference at the monthly scale are provided in Fig. 8. The validation results show that at the monthly scale the ADTC-based framework is able to reduce ΔT_{sb} (i.e., $T_{dm_cloud_free} - T_{dm_true}$) and achieves a higher accuracy than at the daily scale.

At the monthly scale, ΔT_{sb} is around 2.4 K, while MAE for $T_{dm_ATC_DTC}$ is around 0.5 K. The comparison between the sites further indicates that ΔT_{sb} is related to land cover type, e.g., ΔT_{sb} is larger over bare soil (the TBL and DRA sites), which tend to have larger DTRs. This finding is similar to that under cloud-free conditions and can be explained in the same way (see Fig. 4). In contrast, the error of T_{ATC_DTC} remains relatively stable and is insensitive to land cover type. Furthermore, the MAEs of $T_{dm_cloud_free}$ in Fig. 8 generally vary between 1.0 and 5.0 K, which mainly reflects the random occurrence of cloud-free observations (see Section 4.2.1). In contrast, the MAEs of $T_{dm_ATC_DTC}$ are stable at around 0.5 K. This stability mainly results from the temporal continuity obtained with the ADTC-based framework (see Fig. 2), which reduces the uncertainty caused by missing data (e.g., due to clouds) before calculating the monthly mean LST.

Comparisons between the daily and monthly scales (Fig. 7 vs. Fig. 8) indicate that the MAE of $T_{dm_ATC_DTC}$ is generally higher at the daily scale (1.0 K) than at the monthly scale (0.5 K). This finding is expected because the temporal aggregation neutralizes partially positive and negative biases in T_{dm} within a month (Langer et al., 2010), which demonstrates a more accurate and significant ΔT_{sb} reduction over a larger time scale.

4.3. Individual improvements of T_{dm} estimates from the ATC and DTC models

The ATC and DTC models both contribute to the reduction of sampling bias (ΔT_{sb}) and an improved estimate of T_{dm} . To evaluate their individual contributions, we calculate the accuracy improvement due to the ATC and DTC models separately and assess the respective contributions using the six estimates of daily mean LST defined in Table 2.

When compared against T_{dm_true} (i.e., mean LST obtained from hourly observations), the difference between the accuracy of $T_{dm_cloud_free}$ (i.e., the mean of cloud-free observations) and $T_{dm_ATC_four}$ (i.e., the mean of four LSTs at the four satellite overpass times with under-cloud LSTs reconstructed by the ATC model) reflects the contribution of the ATC model, i.e., the difference between the means of ΔT_A and ΔT_B (see Fig. 9). The results show that the ATC model reduces the MAEs of T_{dm} from around 4.2 K (for $T_{dm_cloud_free}$) to 2.0 K (for $T_{dm_ATC_four}$) at the daily scale and from 2.5 K (for $T_{dm_cloud_free}$) to 2.0 K (for $T_{dm_ATC_four}$) at the monthly scale. The reduction in ΔT_{sb} indicates that using under-cloud LSTs reconstructed by the ATC model yields better estimates of T_{dm} .

The difference in accuracy between $T_{dm_cloud_free}$ and $T_{dm_obs_four}$ (i.e., the mean of the four LST actually observed at the four overpass times), shown in Fig. 9 as the difference between the means of ΔT_A and ΔT_C , reflects the maximum reduction in ΔT_{sb} that can be achieved by under-cloud LSTs reconstruction. The assessments show that the use of actual under-cloud LST observations reduces the MAE from 4.2 K (for $T_{dm_cloud_free}$) to 1.6 K (for $T_{dm_obs_four}$) at the daily scale and from 2.5 K (for $T_{dm_cloud_free}$) to 1.6 K (for $T_{dm_obs_four}$) at the monthly scale. Compared with the MAE of $T_{dm_ATC_four}$ (around 2.0 K, shown as ΔT_B in Fig. 9), the use of actual under-cloud LST observations reduces the MAE by 0.4 K, (the difference between the means of ΔT_B and ΔT_C in Fig. 9), which partly reflects the uncertainty introduced by the ATC model (see Section 4.4). However, even with four actual under-cloud LST

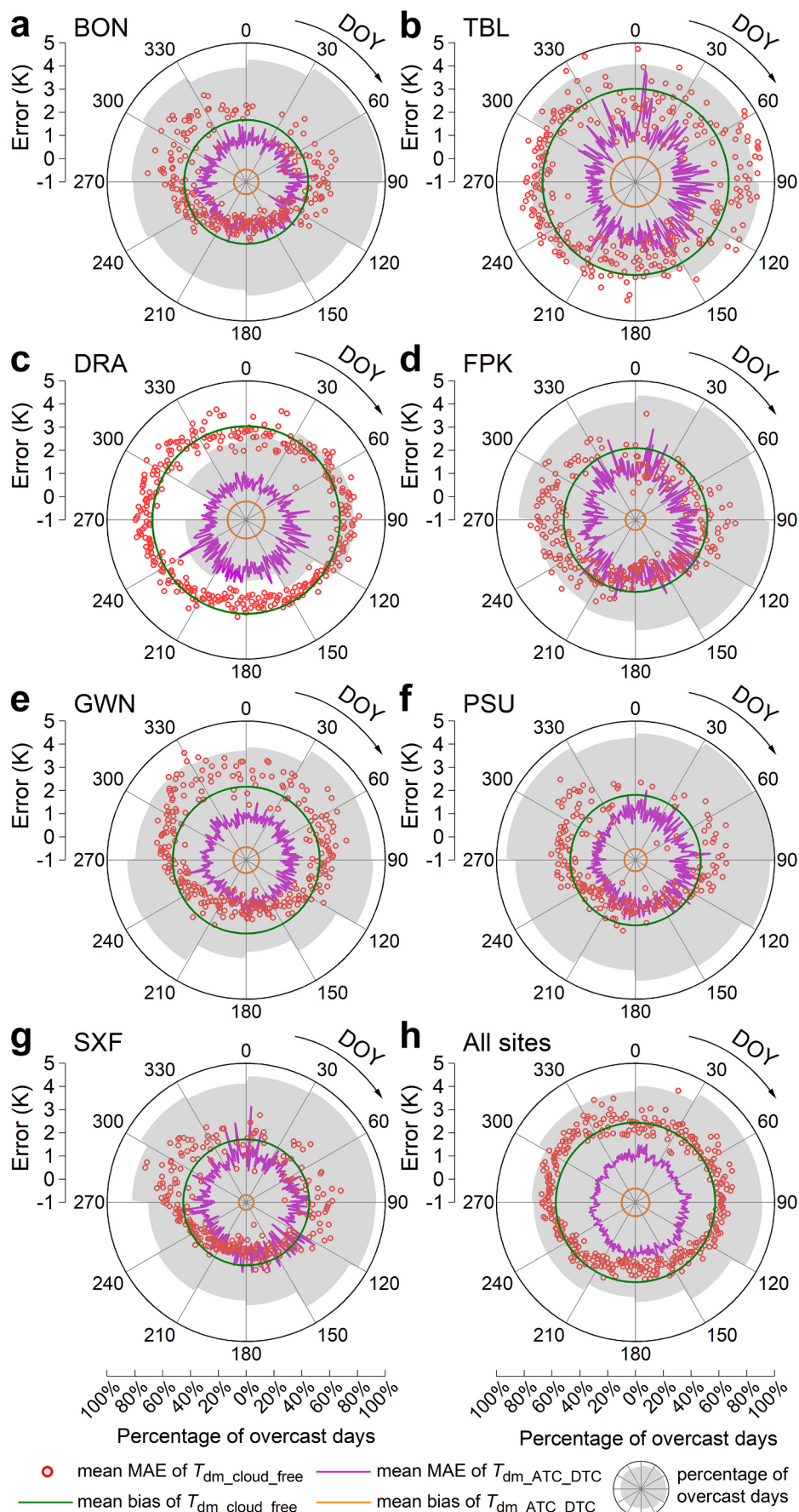


Fig. 7. Errors (represented by the MAE and mean bias) of $T_{dm_cloud_free}$ (red points and green lines) and $T_{dm_ATC_DTC}$ (purple and orange lines) at the daily scale. Errors for each SURFRAD site are presented from (a) to (g) and overall errors for seven sites are presented in (h). The angular and radial coordinates of the polar figures denote the day of year and daily errors, respectively. The error of $T_{dm_cloud_free}$ was calculated based on Case 1 in Fig. 5b. The gray shadow background displays the percentage of overcast days within the 30-day intervals (i.e., Cases 2–16 within the 30-day intervals), with the axis below (g) and (h) indicating the corresponding percentage. (For interpretation of the references to colour in this figure legend, the reader is referred to the web version of this article.)

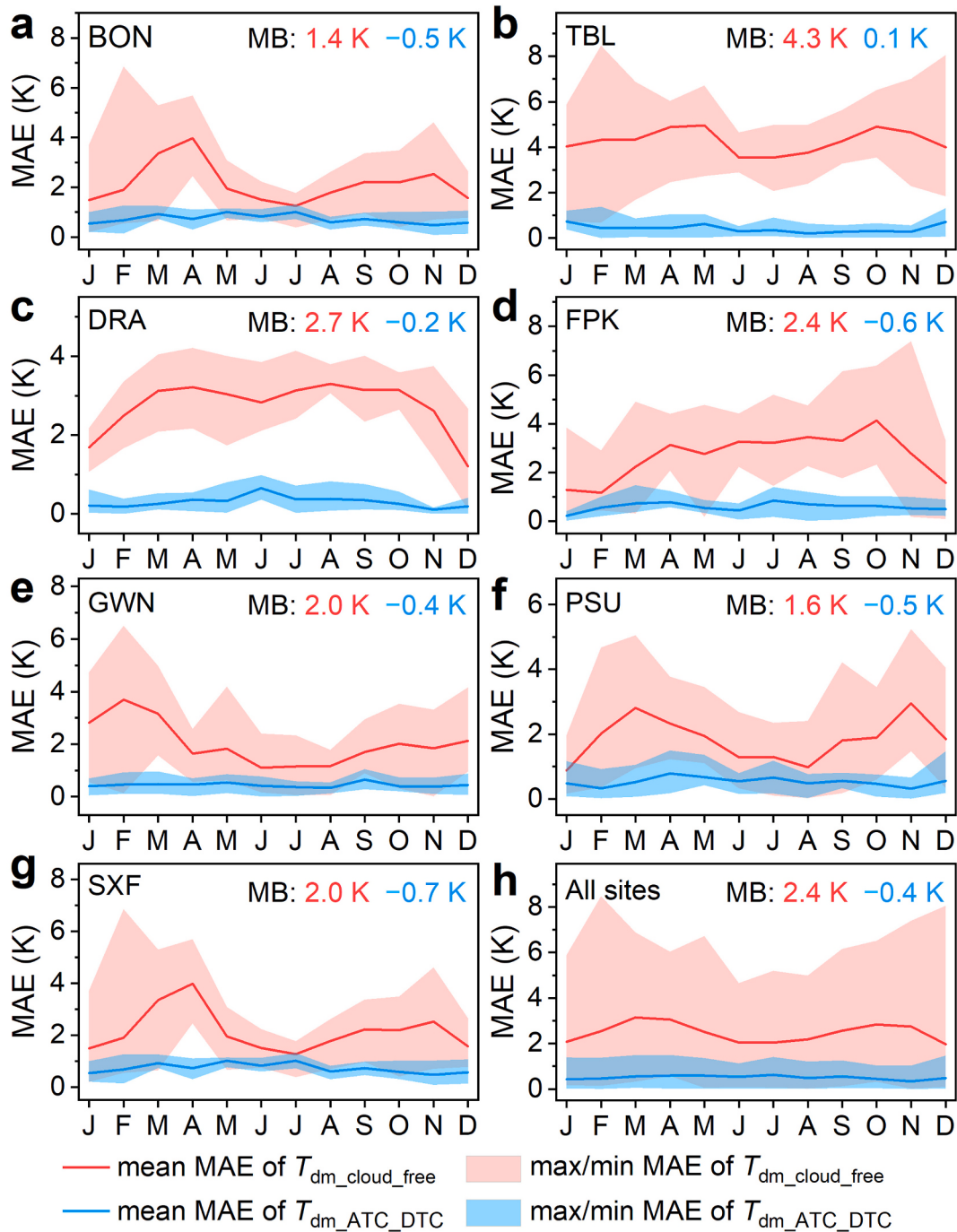


Fig. 8. Errors (represented by MAE and mean bias) of $T_{dm_cloud_free}$ and $T_{dm_ATC_DTC}$ at the monthly scale. Errors at each SURFRAD site are presented from (a) to (g) and overall errors of seven sites are presented in (h).

observations, the MAE of $T_{dm_obs_four}$ (ΔT_C in Fig. 9a and c) is still about 1.6 K at the daily and monthly scales. Over bare soils, the MAEs of $T_{dm_obs_four}$ may become even higher, e.g., up to 2.5 K at TBL and DRA sites at the daily scale. This indicates that estimating T_{dm} as the direct mean of the four LSTs at the overpass times is inaccurate and a more frequent sampling within the diurnal dynamics is necessary.

Employing the ATC model ensures the availability of four valid LSTs per day (see Fig. 2): these then can serve as input to the four-parameter DTC model and for calculating T_{dm} . The contribution of the DTC model can be isolated by comparing the MAEs for $T_{dm_ATC_four}$ (ΔT_B in Fig. 9; only the ATC model is used) and $T_{dm_ATC_DTC}$ (ΔT_D in Fig. 9; the ATC and DTC models are both used). Fig. 9 illustrates that the use of the DTC

model reduces MAE from around 2.0 K (for $T_{dm_ATC_four}$) to 1.0 K (for $T_{dm_ATC_DTC}$) at the daily scale and from 2.0 K (for $T_{dm_ATC_four}$) to 0.5 K (for $T_{dm_ATC_DTC}$) at the monthly scale.

The contribution of the DTC model can also be studied in isolation by comparing the differences in accuracy obtained for $T_{dm_obs_four}$ (i.e., the mean of the four true LST observations per day) and $T_{dm_obs_DTC}$ (for which the DTC model and four actual LST observations per day are combined). In Fig. 9 this corresponds to the differences between means of ΔT_C and ΔT_E : the results show that MAE decreases from around 1.6 K (for $T_{dm_obs_four}$) to 0.8 K (for $T_{dm_obs_DTC}$) at the daily scale and from 1.5 K (for $T_{dm_obs_four}$) to 0.5 K (for $T_{dm_obs_DTC}$) at the monthly scale (see Fig. 9). The similar performance of $T_{dm_obs_DTC}$ and $T_{dm_ATC_DTC}$ (i.e., the

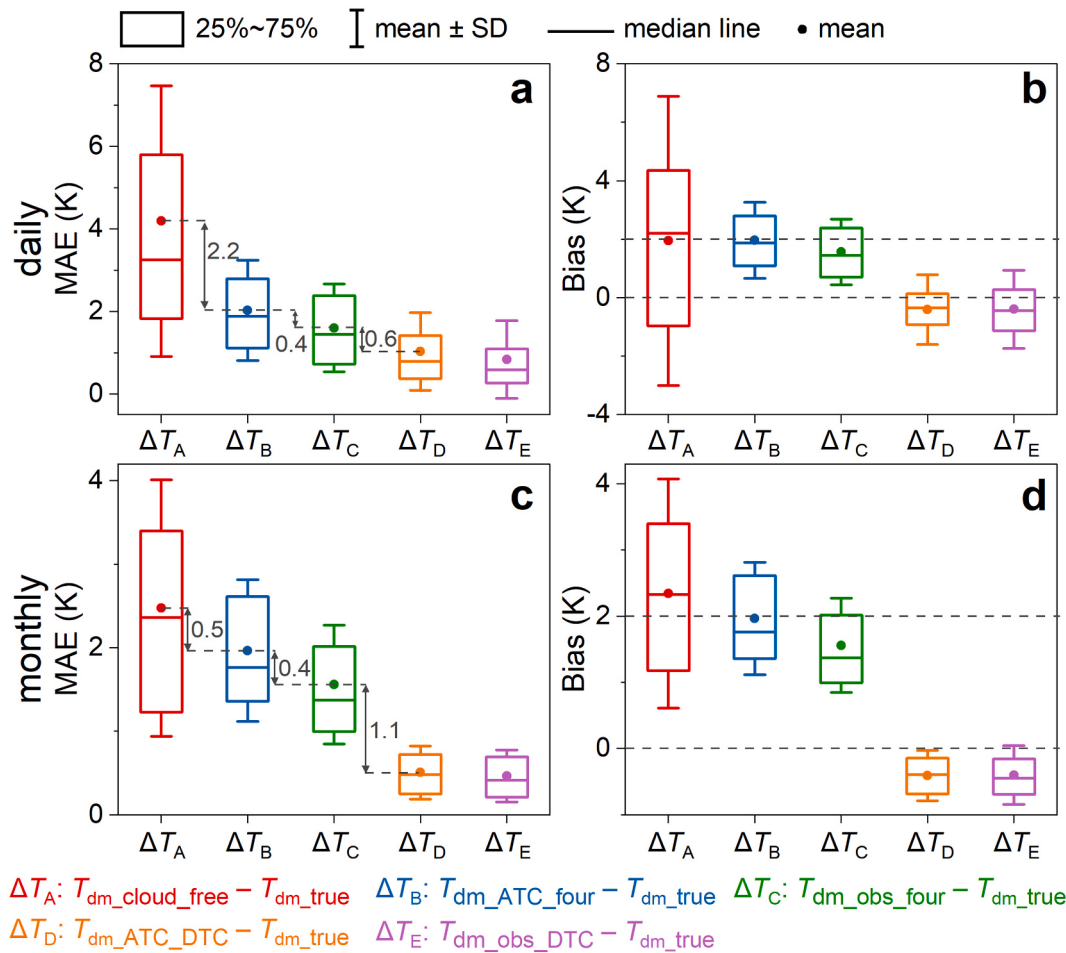


Fig. 9. The separate contributions of the ATC and DTC models in estimating T_{dm} . Differences with respect to T_{dm_true} are shown for $T_{dm_cloud_free}$, $T_{dm_ATC_four}$, $T_{dm_obs_four}$, $T_{dm_ATC_DTC}$, and $T_{dm_obs_DTC}$ (variables are explained in Table 2). Boxplots for MAE and bias at the daily scale are given in (a) and (b), respectively, while (c) and (d) show the respective values at the monthly scale. Errors of $T_{dm_cloud_free}$ at the daily scale are calculated for all the sixteen cases (see Fig. 5).

similarity of ΔT_D and ΔT_E in Fig. 9), where the former performs slightly better at the daily scale but the two getting very close at the monthly scale, demonstrates the robustness of DTC model. In other words, in spite of some bias of the ATC model (see Section 4.4), the ADTC-based framework can still estimate T_{dm} accurately.

In summary, for the data used here and with the MAE of $T_{dm_cloud_free}$ at the daily scale as the baseline, employing the ATC model reduces MAE from 4.2 K to 2.0 K (from ΔT_A to ΔT_B in Fig. 9). When LSTs are first reconstructed with the ATC model, the subsequent use of the DTC model reduces the MAE from 2.0 K to 1.0 K (from ΔT_B to ΔT_D in Fig. 9).

4.4. Uncertainty analysis

Using under-cloud LST observations, i.e., in-situ data, as reference, Fig. 10 displays the monthly MAEs and biases for LSTs obtained with the ATC model during the day and at night: the mean MAE, calculated over all months and all sites, is larger during the day (3.0 K) than at night (1.9 K). Furthermore, the mean bias is positive during the day (2.6 K) but negative at night (-1.1 K). The relatively larger MAE during the day can be explained by the stronger impact of clouds on solar irradiation and, therefore, on daytime LST (Ermida et al., 2019). Considering that clouds usually cool the surface during daytime while they keep it warm at night

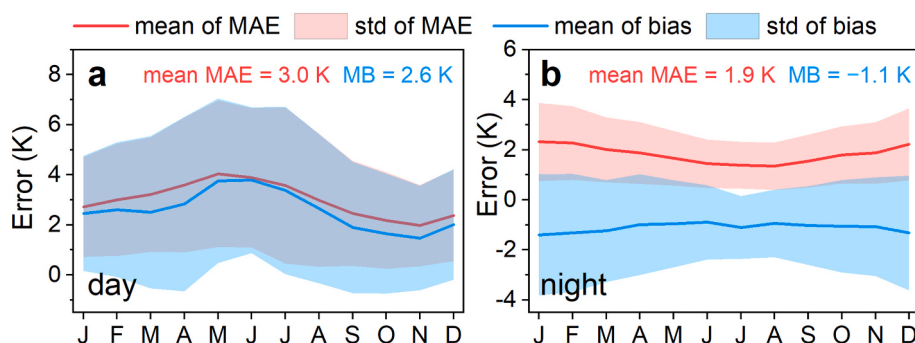


Fig. 10. Monthly MAEs and biases for ATC reconstruction results validated against SURFRAD data. Daytime and nighttime results are given in (a) and (b), respectively. Also provided are the MAE and bias averaged over all months for the seven SURFRAD sites (at the top of each subplot).

(Ermida et al., 2019; Jin, 2000; Liu et al., 2019; Long et al., 2020), a positive (negative) daytime (nighttime) bias is reasonable, since under-cloud LSTs reconstructed from cloud-free observations tend to be overestimated (underestimated) during the day (at night). While the errors of under-cloud LSTs reconstructed with the ATC model are not small, they are acceptable when compared to those obtained with PMW and SEB methods (Duan et al., 2017; Zeng et al., 2018; Zhang et al., 2019). The relatively low accuracy partly results from the limited capability of the ATC model to describe the impact of cloud disturbance, even if surface air temperatures under both cloud-free and overcast conditions are used additionally (Liu et al., 2019; Zou et al., 2018).

Although the instantaneous under-cloud LSTs reconstructed by the ATC model have limited accuracy, the combination of the ATC and DTC models is sufficiently robust for estimating T_{dm} with a significantly higher accuracy under various cloud-contaminated conditions. To assess the robustness of the DTC model to ATC modelling uncertainty and short-term LST fluctuation in estimating T_{dm} , we compare the MAEs of the DTC models in terms of instantaneous temperature (i.e., $T_{in,ATC,DTC}$) as well as daily mean temperature (i.e., $T_{dm,ATC,DTC}$) (Fig. 11). For Cases 1 to 16 (Fig. 5), with the number of invalid LSTs (blocked by clouds) increasing gradually, the MAE of $T_{in,ATC,DTC}$ increases from 1.9 K to 2.4 K; in contrast, the MAE of $T_{dm,ATC,DTC}$ remains relatively stable at around 1.0 K. The relatively larger errors of $T_{in,ATC,DTC}$ (instantaneous temperature) indicate that the used DTC model, which has been developed for clear-sky conditions, is unable to reproduce short term LST fluctuations, e.g., due to clouds. In contrast, the significantly lower MAEs of $T_{dm,ATC,DTC}$ (daily mean temperature) for Cases 1 to 16 demonstrate the robustness when using the DTC model for estimating T_{dm} .

In order to further illustrate the robustness of the DTC modelling in estimating T_{dm} , the comparison between in-situ and modelled LSTs for six typical days characterized by various cloud-contaminated conditions is shown in Fig. 12. In terms of instantaneous LST, the results illustrate that the accuracy of the DTC modelling generally decreases with the increase of cloud contamination, which is understandable in consideration of the clear-sky hypothesis required for the DTC model (Göttsche and Olesen, 2001, 2009; Hong et al., 2018). Besides, the MAE of $T_{in,ATC,DTC}$ is often greater than that of $T_{in,obs,DTC}$ (see Fig. 12d and f in particular), indicating the large impact of the ATC model on the hourly LSTs simulated by the DTC model. By contrast, in terms of daily mean LST, the MAEs of $T_{dm,ATC,DTC}$ (or $T_{dm,obs,DTC}$) are reduced considerably when compared with $T_{in,ATC,DTC}$ (or $T_{in,obs,DTC}$), partly due to the offset effect between positive and negative biases during the day and at night, respectively. Moreover, as for the average error of the six examples (given in Fig. 12), the MAE estimated from $T_{dm,ATC,DTC}$ is even 0.1 K lower than that of $T_{dm,obs,DTC}$. The differences in accuracy between instantaneous and daily mean LSTs indicate that, although the hourly

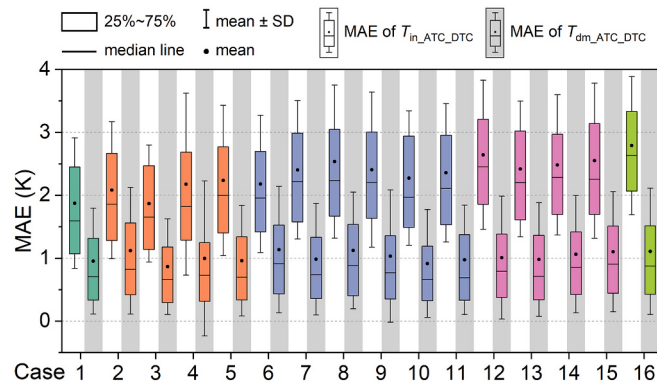


Fig. 11. MAEs of $T_{in,ATC,DTC}$ (on white background) and $T_{dm,ATC,DTC}$ (on gray background) for the sixteen cases in Fig. 5. The five colors represent the number of invalid LSTs at four daily overpass times (between 0 and 4).

LSTs interpolated with the DTC model may be sensitive to short-term LST fluctuations as well as the ATC modelling errors, the estimation of T_{dm} with the ADTC-based framework remains robust even under overcast conditions.

4.5. Discussion

Our analyses have shown that the ADTC-based framework can considerably reduce the sampling bias (ΔT_{sb}) and yields spatiotemporally continuous estimates of T_{dm} under cloud-free and overcast conditions. The framework is easily implemented as it only includes an ATC model and a DTC model. In addition, the framework only requires LST products from tandem polar-orbiters (e.g., from MODIS) and some reanalysis data as inputs; therefore, the framework is globally applicable and independent of location (see Table S2, Figs. S1&S5). Further validations with in-situ LSTs obtained from 115 globally distributed FLUXNET sites (please see Figs. S3 & S4 in the Supplementary Material) are mostly comparable to those with the SURFRAD dataset (Figs. 9 & 10). The MAEs of $T_{dm,ATC,DTC}$ for the FLUXNET sites are mostly less than 1.5 K (Fig. S5 & Table S2), which indicates the global applicability of the ADTC-based framework. Therefore, with adequate computational resources, the ADTC-based framework can be used to generate global 1-km T_{dm} products. However, in order to improve the obtained estimates of global daily mean or even hourly 1-km LSTs, future work on the ADTC-based framework may focus on the following aspects:

- (I) Accuracy improvement: while our results show that T_{dm} accuracy is generally convincing (MAE around 1.0 K at the daily scale), the uncertainty analysis (refer to Section 4.4) reveals that (1) instantaneous under-cloud LSTs reconstructed by the ATC model are still biased and (2) diurnal LST dynamics reconstructed by the DTC model do not describe short-term LST fluctuations due to the limitation of clear-sky hypothesis. In order to reduce the bias of the under-cloud LSTs reconstructed by the ATC model, information on shortwave radiation and cloud cover could be integrated into the framework (Liu et al., 2019; Wang et al., 2020; Zeng et al., 2018; Zhang et al., 2017; Zhao and Duan, 2020). To obtain temporally continuous LSTs of higher accuracy, the DTC model used in this study may be further improved to suit overcast condition, e.g., by incorporating surface variables from reanalysis data or output variables of land surface models (Jin, 2000; Long et al., 2020; Martins et al., 2019; Zhang et al., 2015). However, it should be noted that the ADTC-based framework might become less applicable at the global scale if many auxiliary data or more complex models are incorporated. Therefore, a balance between modelling accuracy and global applicability (or simplicity) should be considered and the design of the T_{dm} estimation framework should consider the application scale at which the T_{dm} are to be obtained (e.g., local vs. global applications).
- (II) Improvement towards global applications: the ADTC-based framework performs nonlinear ATC and DTC modelling on a pixel-by-pixel basis. This indicates that its application on a global (or a very large) scale at the 1 km spatial resolution would be extremely time-consuming. Since each pixel is independent within the calculation, parallel computation is potentially helpful to reduce processing time, but the computation resource may be an issue that needs further consideration. Previous studies have shown that the controlling parameters of the ATC and DTC models (e.g., the daily/annual mean and amplitude in LST) are highly consistent between neighboring pixels within a small area (Bechtel, 2015; Fu and Weng, 2018; Holmes et al., 2013; Zhou et al., 2013), which could be used to improve the algorithm efficiency (Quan et al., 2014). Therefore, exploiting the spatial similarity of some ATC and DTC model parameters can help to significantly reduce the calculation redundancy of the ADTC-based framework. Furthermore, for global applications, the

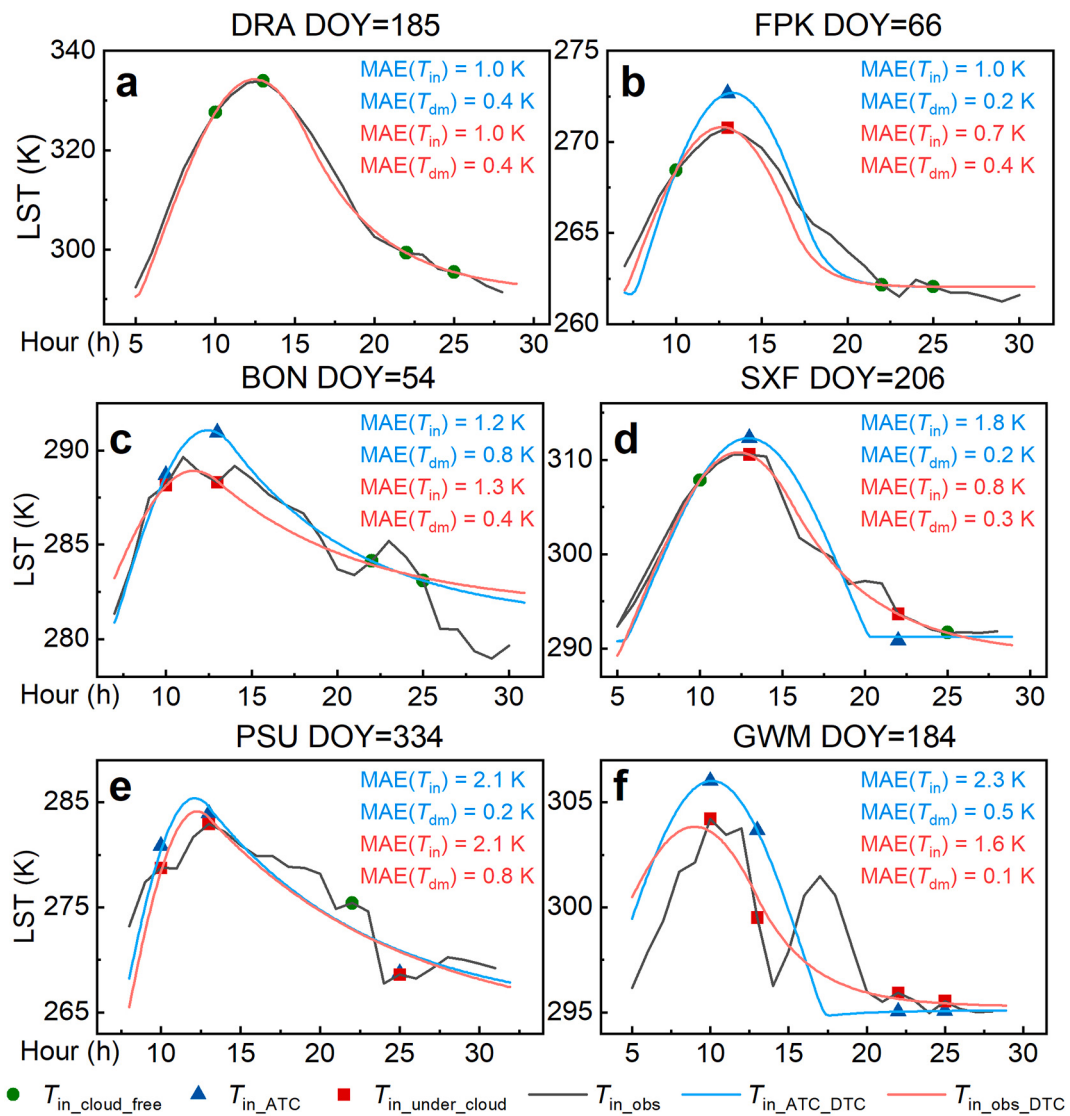


Fig. 12. Typical examples of DTC modelling results obtained for six SURFRAD sites in 2017. The blue (red) numbers in the upper right corners provide the MAEs of $T_{in,ATC,DTC}$ and $T_{dm,ATC,DTC}$ ($T_{in,obs,DTC}$ and $T_{dm,obs,DTC}$). In (a), the conditions are completely cloud-free; therefore, the results for $T_{in,ATC,DTC}$ and $T_{in,obs,DTC}$ are identical (i.e., ATC modelling is not needed). (b)-(f) represent the cases with increasing cloud contamination. (For interpretation of the references to colour in this figure legend, the reader is referred to the web version of this article.)

currently used ATC model may not perform sufficiently well in low-latitude (e.g., tropical) regions. The adjusted ATC models with multiple sinusoidal curves should be more suitable for these regions (Bechtel, 2015; Liu et al., 2019). A similar issue arises for the currently used DTC model in high-latitude regions where the diurnal LST dynamics no longer follows a sinusoidal curve during the daytime and an exponential cooling at night due to the polar day/night phenomenon. For these regions, modified DTC models that consider this phenomenon can be used. In addition, for global LST data from polar orbiters such as MODIS, uncertainties may be further reduced by considering the overpass time fluctuations of sensors as well as surface thermal anisotropy before applying the ADTC-based framework (Duan et al., 2014; Ren et al., 2014).

(III) New LST products: It is anticipated that the ADTC-based framework can be employed to estimate instantaneous (or hourly) LSTs (or daily maximum and minimum LST and DTR) with an acceptable accuracy at the monthly or seasonal scales (i.e., under synthetic cloud-free conditions), mostly because the ATC and DTC models are robust under synthetic cloud-free conditions. At

the daily scale, once the uncertainties of the ATC and DTC models are further reduced as described in (I) and (II), the ADTC-based framework can as well be used to estimate instantaneous (or hourly) LSTs and the associated daily maximum and minimum LST and DTR. However, we need to emphasize that instantaneous LST modelling can be costly and is unnecessary if the goal is to estimate daily maximum and minimum LST (or DTR). In that case, other more efficient approaches can be used, which bypass the costly instantaneous modelling, e.g., an empirical relationship between DTR and the four daily LST observations and some auxiliary data can be employed (Crosson et al., 2012; Duan et al., 2014).

5. Conclusions

Traditional methods to calculate daily (monthly) mean LST (T_{dm}) have a large sampling bias (ΔT_{sb}) when directly averaging cloud-free LSTs from tandem polar orbiters. To reduce the ΔT_{sb} , this study proposed an ADTC-based framework that combines an enhanced ATC model with a four-parameter DTC model and applied it to thermal

observations from tandem polar orbiters. Using geostationary satellite data (FY-2F and MSG-SEVIRI) and in-situ measurements (SURFRAD), the ADTC-based framework was validated under cloud-free and overcast conditions at daily and monthly scales. We additionally analyzed the individual contributions and uncertainties of the ATC and DTC models to the T_{dm} estimates.

Our major findings include the following three aspects. (1) It is usually difficult to obtain four valid daily LSTs from polar orbiters to estimate T_{dm} . Furthermore, T_{dm} obtained by directly averaging cloud-free observations can yield ΔT_{sb} larger than 2.0 K even when four cloud-free LSTs per daily cycle are available. At the monthly scale, direct averaging can also result in positive ΔT_{sb} larger than 2.0 K. (2) The proposed ADTC-based framework is able to reduce ΔT_{sb} considerably and provides spatiotemporally continuous T_{dm} with a MAE of around 1.0 K (0.5 K) at the daily (monthly) scale. (3) The uncertainty analysis shows that the ATC model provides valuable under-cloud LST estimates and is able to reduce the MAE of T_{dm} from around 4.2 K to 2.0 K. The DTC model displays a robust performance and is able to reduce the MAE of T_{dm} further, i.e. for the data examples used here from around 2.0 K to 1.0 K.

When applied to thermal observations from tandem polar orbiters, the ADTC-based framework not only reduces ΔT_{sb} and estimates T_{dm} with an acceptable accuracy, but it also produces spatiotemporally continuous T_{dm} . Furthermore, the framework is readily applied on the global scale, since it is relatively simple and requires few publicly available data as inputs. Despite the already good accuracy towards the estimation of T_{dm} , the developed ADTC-based framework could be further improved by using more complex ATC and DTC models. However, in its current form the framework provides a simple, robust, and sufficiently accurate approach and will be highly useful for many applications requiring T_{dm} as input.

Declaration of Competing Interest

The authors declare that they have no known competing financial interests or personal relationships that could have appeared to influence the work reported in this paper.

Acknowledgements

We are grateful to the following organizations for providing the data used in this research: (1) Global Radiation group of Earth System Research Laboratory Global Monitoring Division managed by the National Oceanic and Atmospheric Administration (NOAA) for providing SURFRAD data, downloaded from <https://www.esrl.noaa.gov/gmd/grd/surfrad/>; (2) Land Processes Distributed Active Archive Center (LP DAAC) managed by the National Aeronautics and Space Administration (NASA) Earth Science Data and Information System (ESDIS) project for providing MOD11A1 and MYD11A1 products, downloaded from [http://ladsweb.nascom.nasa.gov/](https://ladsweb.nascom.nasa.gov/); (3) The Satellite Application Facility (SAF) on Land Surface Analysis (LSA) for providing MSG-SEVIRI data, downloaded from <https://landsaf.ipma.pt/en/>; (4) China Meteorological Administration National Satellite Meteorological Center (CMA NSMC) for providing FY-2F VISSR data, downloaded from <https://www.nsmc.org.cn/en/>; and (5) NASA's Goddard Space Flight Center for providing MERRA-2 data, downloaded from https://disc.gsfc.nasa.gov/datasets/M2I1NXLFO_V5.12.4/summary.

This work is jointly supported by the National Key Research and Development Programs for Global Change and Adaptation under Grant number 2016YFA0600201, the Jiangsu Provincial Natural Science Foundation under Grant BK20180009, the National Natural Science Foundation of China under Grant 41671420, and the Fundamental Research Funds for the Central Universities under Grant 090414380024. We are also grateful for the financial support provided by the National Youth Talent Support Program of China.

Appendix A. Supplementary data

Supplementary data to this article can be found online at <https://doi.org/10.1016/j.rse.2021.112612>.

References

- Anderson, M.C., Norman, J.M., Kustas, W.P., Houborg, R., Starks, P.J., Agam, N., 2008. A thermal-based remote sensing technique for routine mapping of land-surface carbon, water and energy fluxes from field to regional scales. *Remote Sens. Environ.* 112, 4227–4241.
- Bechtel, B., 2015. A new global climatology of annual land surface temperature. *Remote Sens.* 7, 2850–2870.
- Chen, X., Long, D., Hong, Y., Zeng, C., Yan, D., 2017a. Improved modeling of snow and glacier melting by a progressive two-stage calibration strategy with GRACE and multisource data: how snow and glacier meltwater contributes to the runoff of the upper Brahmaputra River basin? *Water Resour. Res.* 53, 2431–2466.
- Chen, X., Su, Z., Ma, Y., Cleverly, J., Liddell, M., 2017b. An accurate estimate of monthly mean land surface temperatures from MODIS clear-sky retrievals. *J. Hydrometeorol.* 18, 2827–2847.
- Coops, N.C., Duro, D.C., Wulder, M.A., Han, T., 2007. Estimating afternoon MODIS land surface temperatures (LST) based on morning MODIS overpass, location and elevation information. *Int. J. Remote Sens.* 28, 2391–2396.
- Crosson, W.L., Al-Hamdan, M.Z., Hemmings, S.N.J., Wade, G.M., 2012. A daily merged MODIS aqua-Terra land surface temperature data set for the conterminous United States. *Remote Sens. Environ.* 119, 315–324.
- Duan, S.-B., Li, Z.-L., Ning, W., Hua, W., Tang, B.H., 2012. Evaluation of six land-surface diurnal temperature cycle models using clear-sky in situ and satellite data. *Remote Sens. Environ.* 124, 15–25.
- Duan, S.-B., Li, Z.-L., Tang, B.-H., Wu, H., Tang, R., 2014. Generation of a time-consistent land surface temperature product from MODIS data. *Remote Sens. Environ.* 140, 339–349.
- Duan, S.-B., Li, Z.-L., Leng, P., 2017. A framework for the retrieval of all-weather land surface temperature at a high spatial resolution from polar-orbiting thermal infrared and passive microwave data. *Remote Sens. Environ.* 195, 107–117.
- Duan, S.-B., Li, Z.-L., Li, H., Götsche, F.-M., Wu, H., Zhao, W., Leng, P., Zhang, X., Coll, C., 2019. Validation of collection 6 MODIS land surface temperature product using in situ measurements. *Remote Sens. Environ.* 225, 16–29.
- Ermida, S.L., Trigo, I.F., DaCamara, C.C., Götsche, F.M., Olesen, F.S., Hulley, G., 2014. Validation of remotely sensed surface temperature over an oak woodland landscape — the problem of viewing and illumination geometries. *Remote Sens. Environ.* 148, 16–27.
- Ermida, S.L., Trigo, I.F., DaCamara, C.C., Jiménez, C., Prigent, C., 2019. Quantifying the clear-sky bias of satellite land surface temperature using microwave-based estimates. *J. Geophys. Res. Atmos.* 124, 844–857.
- Ermida, S.L., Soares, P., Mantas, V., Götsche, F.-M., Trigo, I.F., 2020. Google earth engine open-source code for land surface temperature estimation from the Landsat series. *Remote Sens.* 12, 1471.
- Firozjaei, M.K., Pathololoumi, S., Alavipanah, S.K., Kiavarz, M., Vaezi, A.R., Biswas, A., 2020. A new approach for modeling near surface temperature lapse rate based on normalized land surface temperature data. *Remote Sens. Environ.* 242, 111746.
- Friedl, M.A., McIver, D.K., Hodges, J.C.F., Zhang, X.Y., Muchoney, D., Strahler, A.H., Woodcock, C.E., Gopal, S., Schneider, A., Cooper, A., Baccini, A., Gao, F., Schaaf, C., 2002. Global land cover mapping from MODIS: algorithms and early results. *Remote Sens. Environ.* 83, 287–302.
- Fu, P., Weng, Q., 2016. Consistent land surface temperature data generation from irregularly spaced Landsat imagery. *Remote Sens. Environ.* 184, 175–187.
- Fu, P., Weng, Q., 2018. Variability in annual temperature cycle in the urban areas of the United States as revealed by MODIS imagery. *ISPRS J. Photogramm. Remote Sens.* 146, 65–73.
- Gelaro, R., McCarty, W., Suárez, M.J., Todling, R., Molod, A., Takacs, L., Randles, C.A., Darmenov, A., Bosilovich, M.G., Reichle, R., Wargan, K., Coy, L., Cullather, R., Draper, C., Akella, S., Buchard, V., Conaty, A., da Silva, A.M., Gu, W., Kim, G.-K., Koster, R., Lucchesi, R., Merkova, D., Nielsen, J.E., Partyka, G., Pawson, S., Putman, W., Rienecker, M., Schubert, S.D., Sienkiewicz, M., Zhao, B., 2017. The modern-era retrospective analysis for research and applications, version 2 (MERRA-2). *J. Clim.* 30, 5419–5454.
- Good, E., 2015. Daily minimum and maximum surface air temperatures from geostationary satellite data. *J. Geophys. Res. Atmos.* 120, 2306–2324.
- Götsche, F.M., Olesen, F.S., 2001. Modelling of diurnal cycles of brightness temperature extracted from METEOSAT data. *Remote Sens. Environ.* 76, 337–348.
- Götsche, F.M., Olesen, F.S., 2009. Modelling the effect of optical thickness on diurnal cycles of land surface temperature. *Remote Sens. Environ.* 113, 2306–2316.
- Götsche, F.M., Olesen, F.S., Trigo, I.F., Bork-Unkelbach, A., Martin, M.A., 2016. Long term validation of land surface temperature retrieved from MSG/SEVIRI with continuous in-situ measurements in Africa. *Remote Sens.* 8, 410.
- Guillevic, P., Götsche, F., Nickeson, J., Hulley, G., Ghent, D., Yu, Y., Trigo, I., Hook, S., Sobrino, J.A., Remedios, J., Román, M., Camacho, F., 2018. Land surface temperature product validation best practice protocol Version 1.1. In: Guillevic, P., Götsche, F., Nickeson, J., Román, M. (Eds.), Best Practice for Satellite-Derived Land Product Validation (p. 58): Land Product Validation Subgroup (WGC/C/CEOS). <https://doi.org/10.5067/doc/ceoswgcv/lpv/lst.001>.
- Guillevic, P.C., Biard, J.C., Hulley, G.C., Privette, J.L., Hook, S.J., Olioso, A., Götsche, F.M., Radocinski, R., Román, M.O., Yu, Y., Csizsar, I., 2014. Validation of land surface

- temperature products derived from the visible infrared imaging radiometer suite (VIIRS) using ground-based and heritage satellite measurements. *Remote Sens. Environ.* 154, 19–37.
- Hassan, Q., Bourque, C., Meng, F.-R., Richards, W., 2007. Spatial mapping of growing degree days: an application of MODIS-based surface temperatures and enhanced vegetation index. *J. Appl. Remote. Sens.* 1, 013511.
- Holmes, T., Crow, W., Hain, C., 2013. Spatial patterns in timing of the diurnal temperature cycle. *Hydrol. Earth Syst. Sci.* 17, 3695–3706.
- Holmes, T., Crow, W., Hain, C., Anderson, M., Kustas, W., 2015. Diurnal temperature cycle as observed by thermal infrared and microwave radiometers. *Remote Sens. Environ.* 158, 110–125.
- Hong, F., Zhan, W., Götsche, F.-M., Liu, Z., Zhou, J., Huang, F., Lai, J., Li, M., 2018. Comprehensive assessment of four-parameter diurnal land surface temperature cycle models under clear-sky. *ISPRS J. Photogramm. Remote Sens.* 142, 190–204.
- Hu, L., Brunsell, N.A., 2013. The impact of temporal aggregation of land surface temperature data for surface urban heat island (SUHI) monitoring. *Remote Sens. Environ.* 134, 162–174.
- Hu, L., Sun, Y., Collins, G., Fu, P., 2020. Improved estimates of monthly land surface temperature from MODIS using a diurnal temperature cycle (DTC) model. *ISPRS J. Photogramm. Remote Sens.* 168, 131–140.
- Hu, Y., Zhong, L., Ma, Y., Zou, M., Xu, K., Huang, Z., Feng, L., 2018. Estimation of the land surface temperature over the Tibetan plateau by using Chinese FY-2C geostationary satellite data. *Sensors* 18.
- Huang, F., Zhan, W., Voogt, J., Hu, L., Wang, Z., Quan, J., Ju, W., Guo, Z., 2016. Temporal upscaling of surface urban heat island by incorporating an annual temperature cycle model: a tale of two cities. *Remote Sens. Environ.* 186, 1–12.
- Jin, M., 2000. Interpolation of surface radiative temperature measured from polar orbiting satellites to a diurnal cycle: 2. Cloudy-pixel treatment. *J. Geophys. Res. Atmos.* 105, 4061–4076.
- Jin, M., Dickinson, R.E., 2010. Land surface skin temperature climatology: benefitting from the strengths of satellite observations. *Environ. Res. Lett.* 5, 044004.
- Langer, M., Westermann, S., Boike, J., 2010. Spatial and temporal variations of summer surface temperatures of wet polygonal tundra in Siberia - implications for MODIS LST based permafrost monitoring. *Remote Sens. Environ.* 114, 2059–2069.
- Li, H., Sun, D., Yu, Y., Wang, H., Liu, Y., Liu, Q., Du, Y., Wang, H., Cao, B., 2014. Evaluation of the VIIRS and MODIS LST products in an arid area of Northwest China. *Remote Sens. Environ.* 142, 111–121.
- Li, H., Li, R., Yang, Y., Cao, B., Bian, Z., Hu, T., Du, Y., Sun, L., Liu, Q., 2020. Temperature-based and radiance-based validation of the collection 6 MYD11 and MYD21 land surface temperature products over barren surfaces in northwestern China. *IEEE Trans. Geosci. Remote Sens.* 1–14.
- Li, X., Zhou, Y., Asrar, G.R., Zhu, Z., 2018. Creating a seamless 1 km resolution daily land surface temperature dataset for urban and surrounding areas in the conterminous United States. *Remote Sens. Environ.* 206, 84–97.
- Li, Z.-L., Tang, B.-H., Wu, H., Ren, H., Yan, G., Wan, Z., Trigo, I.F., Sobrino, J.A., 2013. Satellite-derived land surface temperature: current status and perspectives. *Remote Sens. Environ.* 131, 14–37.
- Liang, S., Li, X., Wang, J., 2013. Quantitative Remote Sensing: Concepts and Algorithms. Science Press, Beijing, China.
- Liu, Z., Zhan, W., Lai, J., Hong, F., Quan, J., Bechtel, B., Huang, F., Zou, Z., 2019. Balancing prediction accuracy and generalization ability: a hybrid framework for modelling the annual dynamics of satellite-derived land surface temperatures. *ISPRS J. Photogramm. Remote Sens.* 151, 189–206.
- Long, D., Yan, L., Bai, L., Zhang, C., Li, X., Lei, H., Yang, H., Tian, F., Zeng, C., Meng, X., Shi, C., 2020. Generation of MODIS-like land surface temperatures under all-weather conditions based on a data fusion approach. *Remote Sens. Environ.* 246, 111863.
- Martin, M.A., Ghent, D., Pires, A.C., Götsche, F.-M., Cermak, J., Remedios, J.J., 2019. Comprehensive in situ validation of five satellite land surface temperature data sets over multiple stations and years. *Remote Sens.* 11, 479.
- Martins, J.P.A., Trigo, I.F., Ghilain, N., Jimenez, C., Götsche, F.-M., Ermida, S.L., Olesen, F.-S., Gellens-Meulenberghs, F., Arboleda, A., 2019. An all-weather land surface temperature product based on MSG/SEVIRI observations. *Remote Sens.* 11, 3044.
- Ouyang, B., Che, T., Dai, L., Wang, Z., 2012. Estimating mean daily surface temperature over the Tibetan plateau based on MODIS LST products. *J. Glaciol. Geocryol.* 34, 296–303.
- Quan, J., Wang, J., Li, J., Chen, Y., Zhan, W., Voogt, J., 2014. A hybrid method combining neighborhood information from satellite data with modeled diurnal temperature cycles over consecutive days. *Remote Sens. Environ.* 155, 257–274.
- Quan, J., Zhan, W., Ma, T., Du, Y., Guo, Z., Qin, B., 2018. An integrated model for generating hourly Landsat-like land surface temperatures over heterogeneous landscapes. *Remote Sens. Environ.* 206, 403–423.
- Rao, Y., Liang, S., Wang, D., Yu, Y., Song, Z., Zhou, Y., Shen, M., Xu, B., 2019. Estimating daily average surface air temperature using satellite land surface temperature and top-of-atmosphere radiation products over the Tibetan plateau. *Remote Sens. Environ.* 234, 111462.
- Ren, H., Liu, R., Yan, G., Mu, X., Li, Z., Nerry, F., Liu, Q., 2014. Angular normalization of land surface temperature and emissivity using multiangular middle and thermal infrared data. *IEEE Trans. Geosci. Remote Sens.* 52, 4913–4931.
- Sims, D.A., Rahman, A.F., Cordova, V.D., El-Masri, B.Z., Baldocchi, D.D., Bolstad, P.V., Flanagan, L.B., Goldstein, A.H., Hollinger, D.Y., Misson, L., Monson, R.K., Oechel, W.C., Schmid, H.P., Wofsy, S.C., Xu, L., 2008. A new model of gross primary productivity for north American ecosystems based solely on the enhanced vegetation index and land surface temperature from MODIS. *Remote Sens. Environ.* 112, 1633–1646.
- Sismanidis, P., Keramitsoglou, I., Bechtel, B., Kiranoudis, T.C., 2017. Improving the downscaling of diurnal land surface temperatures using the annual cycle parameters as disaggregation kernels. *Remote Sens.* 9, 23.
- Sobrino, J.A., Julien, Y., 2013. Trend analysis of global MODIS-Terra vegetation indices and land surface temperature between 2000 and 2011. *IEEE J. Sel. Top. Appl. Earth Obs. Remote Sens.* 6, 2139–2145.
- Song, X., Wang, Y., Tang, B., Leng, P., Chuan, S., Peng, J., Loew, A., 2017. Estimation of land surface temperature using FengYun-2E (FY-2E) data: a case study of the source area of the Yellow River. *IEEE J. Sel. Top. Appl. Earth Obs. Remote Sens.* 10, 3744–3751.
- Sun, D., Li, Y., Zhan, X., Houser, P., Yang, C., Chiu, L., Yang, R., 2019. Land surface temperature derivation under all sky conditions through integrating AMSR-E/AMSR-2 and MODIS/GOES observations. *Remote Sens.* 11, 1704.
- Wan, Z., 2014. New refinements and validation of the collection-6 MODIS land-surface temperature/emissivity product. *Remote Sens. Environ.* 140, 36–45.
- Wang, K., Liang, S., 2009. Evaluation of ASTER and MODIS land surface temperature and emissivity products using long-term surface longwave radiation observations at SURFRAD sites. *Remote Sens. Environ.* 113, 1556–1565.
- Wang, K., Zhou, C., 2015. Regional contrasts of the warming rate over land significantly depend on the calculation methods of mean air temperature. *Sci. Rep.* 5, 12324.
- Wang, T., Shi, J., Ma, Y., Letu, H., Li, X., 2020. All-sky longwave downward radiation from satellite measurements: general parameterizations based on LST, column water vapor and cloud top temperature. *ISPRS J. Photogramm. Remote Sens.* 161, 52–60.
- Weng, Q., 2009. Thermal infrared remote sensing for urban climate and environmental studies: methods, applications, and trends. *ISPRS J. Photogramm. Remote Sens.* 64, 335–344.
- Weng, Q., Fu, P., Gao, F., 2014. Generating daily land surface temperature at Landsat resolution by fusing Landsat and MODIS data. *Remote Sens. Environ.* 145, 55–67.
- Westermann, S., Langer, M., Boike, J., 2012. Systematic bias of average winter-time land surface temperatures inferred from MODIS at a site on Svalbard, Norway. *Remote Sens. Environ.* 118, 162–167.
- Williamson, S.N., Hik, D.S., Gamon, J.A., Kavanaugh, J.L., Flowers, G.E., 2014. Estimating temperature fields from MODIS land surface temperature and air temperature observations in a sub-Arctic alpine environment. *Remote Sens.* 6, 946–963.
- Wu, P., Shen, H., Zhang, L., Götsche, F.-M., 2015. Integrated fusion of multi-scale polar-orbiting and geostationary satellite observations for the mapping of high spatial and temporal resolution land surface temperature. *Remote Sens. Environ.* 156, 169–181.
- Xia, H., Chen, Y., Li, Y., Quan, J., 2019. Combining kernel-driven and fusion-based methods to generate daily high-spatial-resolution land surface temperatures. *Remote Sens. Environ.* 224, 259–274.
- Xu, H., Yu, Y., Tarpley, D., Götsche, F., Olesen, F., 2014. Evaluation of GOES-R land surface temperature algorithm using SEVIRI satellite retrievals with in situ measurements. *IEEE Trans. Geosci. Remote Sens.* 52, 3812–3822.
- Xu, S., Cheng, J., 2021. A new land surface temperature fusion strategy based on cumulative distribution function matching and multiresolution Kalman filtering. *Remote Sens. Environ.* 254, 112256.
- Yang, J., Zhou, J., Götsche, F.-M., Long, Z., Ma, J., Luo, R., 2020. Investigation and validation of algorithms for estimating land surface temperature from Sentinel-3 SLSTR data. *Int. J. Appl. Earth Obs. Geoinf.* 91, 102136.
- Yu, W., Ma, M., Yang, H., Tan, J., Li, X., 2019. Supplement of the radiance-based method to validate satellite-derived land surface temperature products over heterogeneous land surfaces. *Remote Sens. Environ.* 230, 111188.
- Zakšek, K., Oštir, K., 2012. Downscaling land surface temperature for urban heat island diurnal cycle analysis. *Remote Sens. Environ.* 117, 114–124.
- Zeng, C., Long, D., Shen, H., Wu, P., Cui, Y., Hong, Y., 2018. A two-step framework for reconstructing remotely sensed land surface temperatures contaminated by cloud. *ISPRS J. Photogramm. Remote Sens.* 141, 30–45.
- Zhan, W., Chen, Y., Zhou, J., Wang, J., Liu, W., Voogt, J., Zhu, X., Quan, J., Li, J., 2013. Disaggregation of remotely sensed land surface temperature: literature survey, taxonomy, issues, and caveats. *Remote Sens. Environ.* 131, 119–139.
- Zhan, W., Zhou, J., Ju, W., Li, M., Sandholt, I., Voogt, J., Yu, C., 2014. Remotely sensed soil temperatures beneath snow-free skin-surface using thermal observations from tandem polar-orbiting satellites: an analytical three-time-scale model. *Remote Sens. Environ.* 143, 1–14.
- Zhan, W., Huang, F., Quan, J., Zhu, X., Gao, L., Zhou, J., Ju, W., 2016. Disaggregation of remotely sensed land surface temperature: a new dynamic methodology. *J. Geophys. Res. Atmos.* 121, 10538–10554.
- Zhang, C., Long, D., Zhang, Y., Anderson, M.C., Kustas, W.P., Yang, Y., 2021. A decadal (2008–2017) daily evapotranspiration data set of 1 km spatial resolution and spatial completeness across the North China plain using TSEB and data fusion. *Remote Sens. Environ.* 262, 112519.
- Zhang, X., Pang, J., Li, L., 2015. Estimation of land surface temperature under cloudy skies using combined diurnal solar radiation and surface temperature evolution. *Remote Sens.* 7, 905–921.
- Zhang, X., Wang, C., Zhao, H., Lu, Z., 2017. Retrievals of all-weather daytime land surface temperature from FengYun-2D data. *Opt. Express* 25, 27210–27224.
- Zhang, X., Zhou, J., Götsche, F., Zhan, W., Liu, S., Cao, R., 2019. A method based on temporal component decomposition for estimating 1-km all-weather land surface temperature by merging satellite thermal infrared and passive microwave observations. *IEEE Trans. Geosci. Remote Sens.* 1–22.
- Zhang, X., Zhou, J., Liang, S., Chai, L., Wang, D., Liu, J., 2020a. Estimation of 1-km all-weather remotely sensed land surface temperature based on reconstructed spatial-seamless satellite passive microwave brightness temperature and thermal infrared data. *ISPRS J. Photogramm. Remote Sens.* 167, 321–344.

- Zhang, Y., Chen, Y., Li, J., Chen, X., 2020b. A simple method for converting 1-km resolution daily clear-sky LST into real LST. *Remote Sens.* 12, 1641.
- Zhao, W., Duan, S.-B., 2020. Reconstruction of daytime land surface temperatures under cloud-covered conditions using integrated MODIS/Terra land products and MSG geostationary satellite data. *Remote Sens. Environ.* 247, 111931.
- Zhao, W., Duan, S.-B., Li, A., Yin, G., 2019. A practical method for reducing terrain effect on land surface temperature using random forest regression. *Remote Sens. Environ.* 221, 635–649.
- Zheng, G., Yang, Y., Yang, D., Dafflon, B., Yi, Y., Zhang, S., Chen, D., Gao, B., Wang, T., Shi, R., Wu, Q., 2020. Remote sensing spatiotemporal patterns of frozen soil and the environmental controls over the Tibetan Plateau during 2002–2016. *Remote Sens. Environ.* 247, 111927.
- Zhou, C., Wang, K., 2016. Land surface temperature over global deserts: means, variability, and trends. *J. Geophys. Res. Atmos.* 121, 14344–14357.
- Zhou, J., Chen, Y., Zhang, X., Zhan, W., 2013. Modelling the diurnal variations of urban heat islands with multi-source satellite data. *Int. J. Remote Sens.* 34, 7568–7588.
- Zou, Z., Zhan, W., Liu, Z., Bechtel, B., Gao, L., Hong, F., Huang, F., Lai, J., 2018. Enhanced modeling of annual temperature cycles with temporally discrete remotely sensed thermal observations. *Remote Sens.* 10, 650.